AGU PUBLICATIONS

JGR

Journal of Geophysical Research: Solid Earth

RESEARCH ARTICLE
10.1002/2012JB009748

Key Points:
- A 3-D model of the modern India-Asia orogen is presented
- The modeling improves the understanding of the deformation of the lithosphere
- Results are consistent with geophysical data and geological observations

Correspondence to:
S. M. Schmalholz,
stefan.schmalholz@unil.ch

Citation:
Lechmann, S. M., S. M. Schmalholz, G. Hetényi, D. A. May, and B. J. P. Kaus (2014), Quantifying the impact of mechanical layering and underthrusting on the dynamics of the modern India-Asia collisional system with 3-D numerical models, *J. Geophys. Res. Solid Earth*, *119*, 616–644, doi:10.1002/2012JB009748.

Received 4 SEP 2012
Accepted 11 DEC 2013
Accepted article online 17 DEC 2013
Published online 17 JAN 2014

Quantifying the impact of mechanical layering and underthrusting on the dynamics of the modern India-Asia collisional system with 3-D numerical models

S. M. Lechmann[1,2], S. M. Schmalholz[3], G. Hetényi[4,5], D. A. May[5], and B. J. P. Kaus[6]

[1]Geological Institute, ETH Zurich, Zurich, Switzerland, [2]Now at armasuisse, Federal Department of Defence, Civil Protection and Sport, Thun, Switzerland, [3]Institute of Earth Sciences, University of Lausanne, Lausanne, Switzerland, [4]Swiss Seismological Service, ETH Zurich, Zurich, Switzerland, [5]Institute of Geophysics, ETH Zurich, Zurich, Switzerland, [6]Institute of Geosciences, Center for Computational Sciences and Geocycles Research Center, Johannes Gutenberg University of Mainz, Mainz, Germany

Abstract The impact of mechanical layering and the strength of the Indian lower crust on the dynamics of the modern India-Asia collisional system are studied using 3-D thermomechanical modeling. The model includes an Indian oceanic domain, Indian continental domain, and an Asian continental domain. Each domain consists of four layers: upper/lower crust, and upper/lower lithospheric mantle. The Tarim and Sichuan Basins are modeled as effectively rigid blocks and the Quetta-Chaman and Sagaing strike-slip faults as vertical weak zones. The geometry, densities, and viscosities are constrained by geophysical data sets (CRUST2.0, gravity, and seismology). Both static (no horizontal movement of model boundaries) and dynamic scenarios (indentation) are modeled. It is demonstrated that 3-D viscosity distributions resulting from typical creep flow laws and temperature fields generate realistic surface velocities. Lateral variations in the gravitational potential energy cause locally significant tectonic overpressure (i.e., difference between pressure and lithostatic pressure) in a mechanically strong Indian lower crust (up to ~500 MPa for the static scenario and ~800 MPa for the dynamic scenario). Different density distributions in the lithosphere as well as different viscosities (3 orders of magnitude) in the Indian lower crust cause only minor differences in the surface velocity field. This result suggests that surface velocities alone are insufficient to infer the state of mechanical coupling of the lithosphere. Model results are in agreement with GPS velocities for Indian lower crustal viscosities of 10^{21}–10^{24} Pa s, for a strong Quetta-Chaman Fault (10^{22} Pa s) and a weak Sagaing Fault (10^{20} Pa s).

1. Introduction

The modern India-Asia collisional system and the Tibetan Plateau have been studied intensely to better understand continental tectonics [e.g., *Argand*, 1924; *Gansser*, 1964; *Molnar and Tapponnier*, 1975; *Allegre et al.*, 1984; *Burg and Chen*, 1984; *Patriat and Achache*, 1984; *Beaumont et al.*, 2001; *DeCelles et al.*, 2002; *Royden et al.*, 2008]. However, the understanding of the geodynamic processes and of the evolution of this system remains incomplete. Open questions concern (1) the driving forces of the India-Asia orogeny (e.g., ridge push, slab pull, or slab suction [*Lithgow-Bertelloni and Richards*, 1998; *Conrad and Lithgow-Bertelloni*, 2004]), (2) the style of deformation in different regions of the orogen (e.g., underthrusting, diffusive thickening, or localized deformation along strike-slip faults [e.g., *Tapponnier and Molnar*, 1976; *England and Houseman*, 1986; *Nabelek et al.*, 2009]), (3) the rheology and mechanical behavior of the continental lithosphere (e.g., strong or weak lower crust and/or lithospheric mantle and mechanically coupled or decoupled lithosphere [e.g., *Clark and Royden*, 2000; *Flesch et al.*, 2001; *Jackson*, 2002; *Afonso and Ranalli*, 2004; *Burov*, 2010; *Copley et al.*, 2011]), and (4) the mechanism of plateau formation (e.g., mantle delamination, crustal flow, and thickening [e.g., *England and Houseman*, 1986; *Houseman and England*, 1986; *Molnar et al.*, 1993; *Clark and Royden*, 2000]).

Over the last three decades so-called thin viscous sheet models have frequently been used to explain continental tectonic deformations such as the India-Asia collision [*England and McKenzie*, 1982; *England and Houseman*, 1986; *Houseman and England*, 1986; *Flesch et al.*, 2001; *Dayem et al.*, 2009a; *Ghosh et al.*, 2009]. Although thin viscous sheet models (1) assume vertical boundaries between geological units (e.g., Indian and Asian crust), (2) assume that horizontal velocities are constant with depth, and (3) consider only viscous

rheologies, these models have been useful in better understanding and quantifying the dynamics of the India-Asia orogeny [e.g., *England and McKenzie*, 1982; *England and Houseman*, 1985; *Houseman and England*, 1986; *Vergnolle et al*., 2007; *Dayem et al*., 2009b]. Thin-sheet models have successfully (1) explained crustal thickening as a result of indentation [e.g., *England and McKenzie*, 1982; *England and Houseman*, 1986; *Houseman and England*, 1986], (2) predicted the first-order pattern of observed surface velocities [e.g., *Flesch et al*., 2001; *Vergnolle et al*., 2007], and (3) estimated the effective lithospheric viscosities using estimates of the distribution of gravitational potential energy (GPE) [e.g., *England and Molnar*, 1997a; *Flesch et al*., 2001]. In this study, we investigate the impact of the mechanical layering of the lithosphere and the impact of the strength of the underthrusting Indian lower crust on the three-dimensional (3-D) deformation of the modern India-Asia collisional system. Since typical thin-sheet models are not suitable to investigate vertical variations in velocities and strain rates [*Medvedev and Podladchikov*, 1999a, 1999b; *Lechmann et al*., 2011], we utilize full 3-D numerical models with a similar vertical strength profile as has been used by thin viscous sheet models. Our 3-D model elaborates on the thin-sheet model by resolving vertical changes in strength, and therefore allowing for horizontal velocities that vary with depth. However, we keep two main features of the thin viscous sheet model, namely vertical boundaries between geological units and viscous only rheology. There are four primary aims of our modeling study: First, we aim to quantify the impact of vertical strength variations, particularly due to underthrusting, on the 3-D distribution of velocity, strain rate, and stress. Such quantification is important, for example, to assess the feasibility and accuracy of using surface GPS velocities for predicting subsurface deformations [*Flesch et al*., 2005; *Wang et al*., 2008a] or for determining whether the continental lithosphere is mechanically coupled or decoupled [*Jackson*, 2002; *Beaumont et al*., 2004; *Clark et al*., 2005; *Copley et al*., 2011; *Lechmann et al*., 2011; *Flesch and Bendick*, 2012]. Second, we aim to quantify the 3-D stress and pressure fields for an underthrusting scenario. Third, we aim to develop a quasi-dynamic 3-D model that reproduces the first-order observations of the modern India-Asia collisional system, for example, gravity anomalies, surface velocities, topographic, and seismic sections. Fourth, we aim to verify whether the applied viscosity profiles and variations of the GPE result in realistic velocities and stresses. Such tests allow constraining the viscosities and rheology of the lithosphere for the considered model configuration.

The applied 3-D model considers temperature-dependent viscosities based on experimentally derived flow laws, the mechanical layering of the lithosphere (upper and lower crust, upper and lower lithospheric mantle), three lithospheric domains (Indian oceanic, Indian continental, and Asian continental lithosphere), and takes surface topography into account. The model configuration also comprises the Tarim and the Sichuan Basins and the deformable Indian indenter consisting of layered continental and oceanic lithosphere (Figure 1). Considering a multilayered and deformable Indian indenter is novel with respect to recent 3-D models of the India-Asia collision, which assume a rigid indenter [*Liu and Yang*, 2003; *Yang and Liu*, 2009]. We consider a deformable Indian indenter to move the model boundaries away from the collision zone where the Indian lower crust is bending and underthrusting, so that the results around the collision zone are less affected by the boundary conditions. Because of the application of a deformable Indian indenter we also consider the Quetta-Chaman and the Sagaing strike-slip faults as vertical weak zones.

We configure a geodynamic model, which resembles the present-day structure of the India-Asia collisional system by using geophysical data. The model geometry is primarily based on the CRUST2.0 data set [*Laske et al*., 2002]. Density is constrained by comparing observed Bouguer anomalies (see compilation in *Hetényi* [2007] and *Hetényi et al*. [2007]) on and around the Tibetan Plateau with the gravity signal of the model. Finally, we apply typical flow laws for the continental lithosphere [*Carter and Tsenn*, 1987; *Ranalli*, 1995; *Afonso and Ranalli*, 2004; *Afonso et al*., 2007] and test whether the resulting viscosities and stresses are in agreement with previously published estimates derived from gravitational potential energy (GPE) caused by variations in topography [e.g., *Ghosh et al*., 2006, 2009].

We perform five time steps (each is 500 years yielding 2500 years in total) to calculate the present-day velocity, strain rate, and stress fields to study the 3-D deformation [e.g., *Becker*, 2006]. We consider two model scenarios: The first scenario considers gravity as the only driving force, and deformation is due to the equilibration of lateral variations in GPE. We refer to this type of flow as "density driven". In a second scenario, the model is shortened horizontally, and we investigate the predicted velocity, strain rate, and stress field in terms of lateral and vertical variations. Different model and material parameters are tested in order to assess their relative importance and their impact on the deformation field.

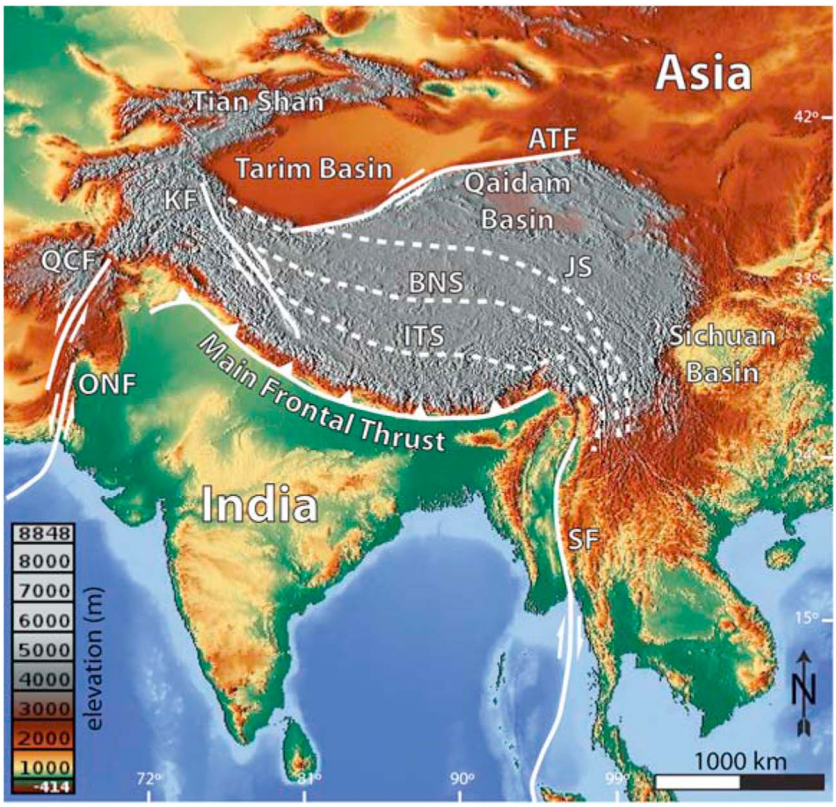

Figure 1. Structural elements map of India, Asia, and the Tibetan Plateau [e.g., *DeCelles et al*., 2002; *Cook and Royden*, 2008]. Background is an elevation map (http://maps-for-free.com). The grey highly elevated area represents the Tibetan Plateau. The dashed lines are the main sutures between the terranes composing the Tibetan Plateau (ITS: Indus-Tsangpo Suture, BNS: Bangong-Nujiang Suture, and JS: Jinsha Suture). Major strike-slip faults are the Quetta-Chaman Fault (QCF), the Sagaing Fault (SF), which are included in the model, and the Karakorum Fault (KF), the Altyn Tagh Fault (ATF), and the Ornach-Nal Fault (ONF) which were not included in the model. The Tarim and the Sichuan Basins are included in the model as rigid obstacles.

2. Methods

The numerical thermomechanical simulations were performed using the parallel 3-D finite element code Lithosphere and Mantle Evolution Model (LaMEM) [*Schmeling et al*., 2008; *Lechmann et al*., 2011]. The governing equations, the definitions of stresses and pressure, and the discretization of the equations are presented in detail in *Lechmann et al*. [2011], and a short summary is given in the Appendix A.

2.1. Model Configuration and Boundary Conditions

The model geometry is based on the CRUST2.0 data [*Laske et al*., 2002]. For a model including India and the Tibetan Plateau data from 0°N–60°N and 61°E–121°E are considered. The topography and the depths of the upper crust, middle crust, and lower crust are used to define the crustal geometry. We only distinguish between an upper and lower crust in our model and, therefore, either the upper and middle crust of CRUST2.0 are combined to form the upper crust or the middle and lower crust are combined to form the lower crust (see section 3.4.1), which ensures that the layers in the numerical models are resolved with a sufficiently high numerical resolution. The upper lithospheric mantle has a uniform thickness of 22 km, and the lower lithospheric mantle reaches down to a depth of 200 km. Since the compilation of CRUST2.0, new data have been acquired, and more accurate Moho depths are available at certain locations. Therefore, we have used the latest seismological profiles through the Tibetan Plateau to complement the CRUST2.0 data set (Figure 2a) and to update Moho depths. Published seismological data of the area of the Tibetan Plateau of the last 15 years were digitized, referenced to sea level and added to the Moho depths of CRUST2.0 (Figure 2b). The CRUST2.0 data were adapted by interpolating the Moho depths between the different profiles, which results in a Moho that is locally up to 20 km deeper than in the CRUST2.0 data set (Figure 2c), resulting in a

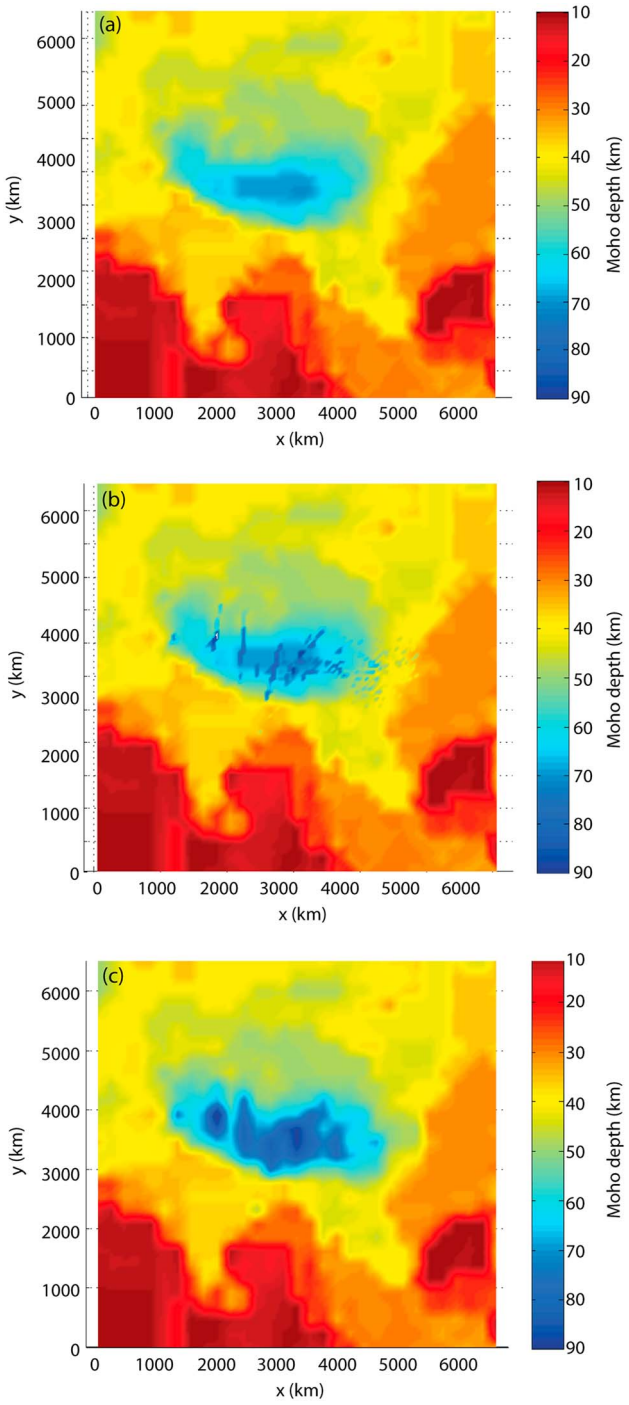

Figure 2. Adapting the CRUST2.0 Moho depths below the Tibetan Plateau. (a) Original CRUST2.0 Moho depths, maximum depth is 70 km. (b) Original CRUST2.0 Moho depths with digitized Moho depths from seismological profiles. (c) Adapted Moho depths including the laterally linearly interpolated seismological profiles, maximum depth is 90 km.

maximum depth of 90 km. The data of the following publications were used to update the Moho depths: *Acton et al.* [2010], *Hauck et al.* [1998], *Kind et al.* [2002], *Li and Mashele* [2009], *Nabelek et al.* [2009], *Rai et al.* [2006], *Robert et al.* [2010], *Schulte-Pelkum et al.* [2005], *Shi et al.* [2004], *Singh et al.* [2010], *Vergne et al.* [2002], *Wang et al.* [2010], *Wittlinger et al.* [2004a, 2004b], *Zhang et al.* [2009], *Zhao et al.* [2010], and B. Zurek and A. Meltzer (personal communication, 2011).

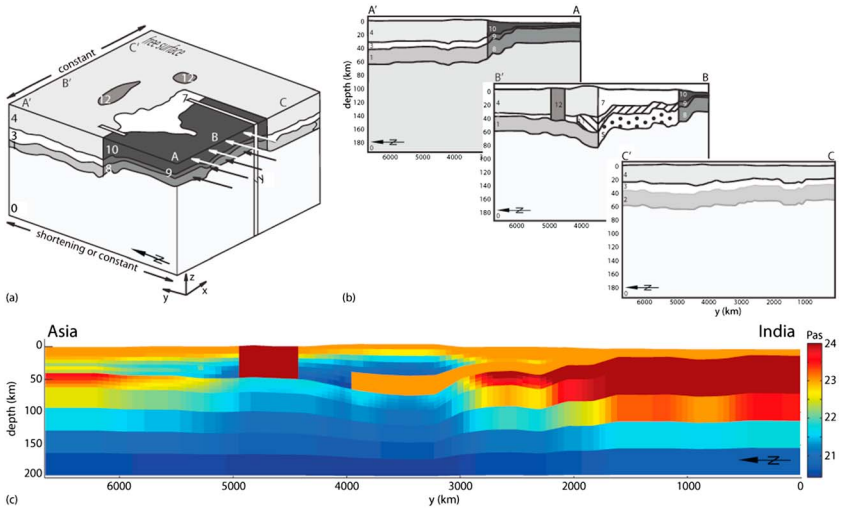

Figure 3. (a) Three-dimensional model, (b) schematic north-south profiles, and (c) north-south section along B-B′ showing the logarithm of the viscosity, resulting from flow laws typically employed for continental lithospheres and the underthrusting Indian lower crust with a viscosity of 10^{23} Pa s. Model dimensions are 6660 km × 6660 km × 200 km. The model includes 14 different material phases (0–13; see also Table 2), which represent the model domains of oceanic and continental India and continental Asia. Each domain consists of four layers (lower and upper lithospheric mantle, lower and upper crust). Furthermore, the Asian continent also includes the Tarim Basin and the Sichuan Basin (phase 12), and the Indian continental lower crust includes a denser eclogitized part (phase 11) [e.g., *Hetényi et al*., 2007]. The thin zones in Figure 3a represent the Quetta-Chaman Fault and the Sagaing Fault, modeled as mechanically weak zones. Between the longitudes (*x* direction) of these two faults, India is being indented into Asia (black and white arrows).

Based on current plate tectonic data [e.g., *Bird*, 2003], the four layers adopted in the model are laterally subdivided into an Indian oceanic domain, an Indian continental domain, and an Asian continental domain (Figure 3a). These domains and their boundaries represent a simplified tectonic setting of the area, with the aim of distinguishing between mechanically distinct domains and not necessarily corresponding to the geological "truth". Lateral boundaries between model units are simplified and assumed to be vertical. Boundaries between oceanic and continental domains correspond with coastlines. The boundary between the Indian and Asian domain is the Main Frontal Thrust at the surface and further north in the lower crust and lithospheric mantle (see description of underthrusting below). This simplified boundary between continents was chosen in order to include both horizontal and vertical heterogeneities in the model. The separation between oceanic and continental India allows defining a more rigid oceanic lithosphere. This is necessary in order to apply the velocity boundary conditions away from the continent, so that the continent is pushed by the oceanic part of the plate. This corresponds to the situation where plate movement originates at a mid-oceanic ridge as there is no continuous slab pulling India down in the central part of Tibet. In addition, the Quetta-Chaman Fault and the Sagaing Fault [*Molnar and Tapponnier*, 1975] are included as weak zones (Figure 1). Incorporating these strike-slip faults allows for a more physically realistic mechanism to accommodate the northward movement of the Indian continent, sliding along these weak zones, compared to using free slip boundaries at the sides of the model domain. The weak zones are four elements wide (≈ 200 km) and extend throughout the entire depth of the model. As the viscosity of the lower lithospheric mantle has a similar viscosity as the weak zones, they only affect the upper lithospheric mantle and the crustal layers (earthquake epicenters along the Sagaing Fault reach down to > 100 km [*U.S. Geological Survey*, 2012]). Furthermore, the Tarim and the Sichuan Basins are included in the crust as effectively rigid blocks (viscosity of 10^{24} Pa s) [*Molnar and Tapponnier*, 1981], and the Indian continental lower crust includes a denser eclogitized component, which underthrusts the Asian upper crust (Figure 3b) [*Hetényi et al*., 2007; *Nabelek et al*., 2009]. The eclogitized lower crustal layer beneath the Tibetan Plateau is a well-constrained, laterally continuous structure over most of Southern Tibet: It is present underneath western [*Wittlinger et al*., 2009], central [*Nabelek et al*., 2009], eastern (International Deep Profiling of Tibet and Himalaya [e.g., *Hauck et al*., 1998] and Namche Barwa (Zurek and Meltzer, personal communication) experiments) Tibet. Since its density is much higher than that of the crust [*Hetényi et al*., 2007], and its rheology is also different from the neighboring layers, including this layer influences the behavior of the model. Furthermore, since the eclogite layer

Table 1. Material Parameters Employed for the Different Phases to Calculate the Temperature-Dependent Viscosity[a]

Layer (Phase)	Preexponential Factor A ($Pa^{-n} s^{-1}$)	Power Law Exponent n	Activation Energy E (J/mol)	Thermal Conductivity k (W/(mK))	Heat Capacity c ($m^2 s^{-2} K^{-1}$)	Radioactive Heat H (W/m^3)
Mantle (0, 1, 2, 5, 8)	2.00E-21	4	471,000	3	1,050	0
Lower crust (3, 6, 9)	3.20E-20	3	276,000	2.1	1,050	4.00E-07
Upper crust (4, 7, 10)	3.16E-26	3.3	190,000	2.5	1,050	1.40E-06
Eclogite (11)	8.80E-22	4.2	445,000	3	1,050	0

[a]Parameters used for the mantle correspond to the wet mantle rheology from *Afonso and Ranalli* [2004]. For the lower crust, parameters for diabase are employed, and for the upper crust the parameters for granite are used [*Burg and Podladchikov*, 1999]. For the eclogitized underthrusting Indian lower crust, parameters for a mafic granulite [*Afonso and Ranalli*, 2004] are employed. In order to avoid unrealistically high viscosities at low temperatures, an upper viscosity cutoff of 10^{26} Pa s was employed.

is present where India underthrusts Tibet, and not on the Asian side, this feature is strongly related to the most recent collision event and therefore is likely to influence the present-day dynamics.

In order to implement a realistic viscosity distribution (Figure 3c), a temperature-dependent, and thus depth-dependent, viscosity is employed:

$$\mu = A^{-\frac{1}{n}} \cdot \dot{\varepsilon}_{II}^{\frac{1}{n}-1} \exp\left(\frac{E}{nRT}\right), \quad (1)$$

where μ is viscosity, A is the preexponential factor, $\dot{\varepsilon}_{II}$ is the square root of the second invariant of the strain rate tensor (see Appendix A), E is the activation energy, R is the universal gas constant ($R = 8.3144621$ J/mol/K), n is the power law stress exponent, and T is the temperature. Thermal boundary conditions are 10°C at the surface and 1300°C at the bottom, which are typical values assumed for a continental lithosphere [*McKenzie et al*., 2005]. We assume zero heat flux on the lateral boundaries of the model. In order to obtain an initial temperature field, which is necessary to assign realistic viscosities, we solve the temperature equation forward in time assuming a thermal age of 400 Myr [e.g., *Burov et al*., 1993]. The laterally variable layer depths and the thermal parameters (Table 1) applied in the different model units lead to different thermal structures of India and Asia, with generally lower temperatures below India. The temperature-dependent flow laws involve a power law dependence on strain rate, which requires performing nonlinear iterations during the solution of the system of equations. As these iterations are time consuming, to obtain a good convergence of two subsequent solutions, we adopted a simplification for many of our simulations: the square root of the second invariant of the strain rate tensor ($\dot{\varepsilon}_{II}$) was fixed for equation (1) to $10^{-15}\,s^{-1}$ which implies that in our models the variation of viscosity with depth due to temperature is taken into account, but that the variations due to strain rate are ignored. Although such strain rate dependence is important (as shown in early thin-sheet studies, e.g., *Houseman and England* [1986]), our models nevertheless show the variations that are observed in nature as we vary the rheological structure of the lithosphere between subsequent simulations. Nevertheless, to quantify the impact of ignoring nonlinearities, three simulations with power law iterations were performed and are discussed in subsection 3.4.3.

Two different velocity boundary conditions (BC) are employed. (BC1): In the first set of simulations gravity is the only driving force, and flow is induced by the equilibration of lateral variations in GPE [*Molnar and Lyon-Caen*, 1988; *Flesch et al*., 2001; *Ghosh et al*., 2006, 2009]. All lateral boundaries have a no-slip condition (zero normal velocity and tangential velocity), the bottom boundary is free slip (zero normal velocity and zero tangential stress), and the top boundary is a free surface (zero normal stress). The lateral boundaries are, therefore, constrained so that they do not move horizontally. In our finite element calculations, the mesh conforms to the surface topography which simulates, in combination with natural boundary conditions of the FEM, a true free surface (stress-free) condition. This is important to investigate gravitationally induced stresses and velocity fields and to place a constraint on viscosities (see section 2.3). (BC2): In the second set of simulations an indenting velocity is applied at the southern lateral boundary, which therefore moves horizontally (Figure 3a, black and white vectors). Between the longitudes (x directions) of the two weak zones, representing the Quetta-Chaman Fault and the Sagaing Fault, a northward velocity of 10 cm/yr is applied along the Indian oceanic domain, from the surface down to the upper lithospheric mantle. This boundary velocity generates an indenting velocity of approximately 4 cm/yr around the continental boundary between India and Asia, consistent with GPS data measured relative to Eurasia [*Zhang et al*., 2004]. As the impact of the underthrusting Indian lower crust underneath the Tibetan Plateau is studied, a deformable indenter is

considered, and thus, the boundaries of the model domain have to be far away from the investigated collision zone. Due to the deformable Indian indenter, the applied indenting boundary conditions imply that there is a gradient in velocity over India, but one aim of this study was to observe the effect of a deformable indenter (particularly for the Indian lower crust), especially around the Himalayan front (see section 3.4.3 and Figure 9). Furthermore, GPS velocities of the Indian plate show slight north-south variations [e.g., *Kreemer et al*., 2003; *Banerjee et al*., 2008]. Resulting model strain rates within India range between $4 \times 10^{-16}\,s^{-1}$ and $10^{-15}\,s^{-1}$ (Figures 10a, 10b, 11c, and 11d) which closely approximate strain rates of $\sim 7 \times 10^{-9}\,year^{-1}$ ($\sim 2 \times 10^{-16}\,s^{-1}$) inferred by *Paul et al*. [2001].

The time step used was 500 years, and we performed five time steps to simulate the present-day deformation field, which is necessary as the incorporation of a free surface requires a slight isostatic adjustment of the model at the beginning of the simulation. In addition, simulations with more time steps (100 time steps ≈ 50,000 years) were performed which confirmed that our results are robust.

The presented model with dimensions of 6660 km × 6660 km × 200 km is resolved with 257 × 257 × 33 nodes (128 × 128 × 16 Q_2P_{-1} elements), and simulations were performed using 256 CPUs. While such a resolution seems low compared to mantle convection models, the techniques used in mantle convection cannot be used to investigate the physical problem of this study. Convection models do typically not permit either topography (horizontal variations in the model height) to be introduced or allow for a stress-free boundary condition to be modeled. Here we use a high-order, body-fitted finite element method. This choice of discretization permits topographic variations to be introduced and allows a free surface boundary condition to be applied and allows material interfaces (such as the Moho) to be accurately discretized. Performing three-dimensional simulations, using these stable high-order finite elements, with a model possessing discontinuous viscosity structures requires specialized multigrid preconditioners. Collectively, the mentioned points make the method used here much more expensive in terms of memory and CPU time than any staggered grid finite difference method used in the convection community. However, the gain is that we do not need extremely fine meshes to resolve material interfaces. Another issue, which further increases the computational cost of the model, is that the viscosity is discontinuous across elements. As such, the solution of the discrete Stokes system becomes much more challenging compared to the temperature-dependent rheologies used in convection models where the variations in viscosity between cells is continuous. Yet, these jumps in viscosity between, for example, the upper and lower crust can have important dynamic consequences, e.g., resulting in channel flow [*Beaumont et al*., 2001].

2.2. Constraining Density

The density distribution is constrained by comparing the gravity signal of the model with observed Bouguer anomalies of the Tibetan Plateau (see compilation in *Hetényi* [2007] and *Hetényi et al*. [2007]). For this purpose, a constant density is assigned to each material phase, and the vertical attraction of gravity is calculated [*Blakely*, 1996]. Since Bouguer anomalies are used for comparison, we use $\Delta\rho = \rho_{ref} - \rho_{fit}$ where ρ_{ref} is a reference density close to the PREM (Preliminary Reference Earth Model) [*Dziewonski and Anderson*, 1981], and ρ_{fit} is the actual value for the calculation of the gravity signal. The applied reference densities are listed in Table 2.

In Table 2 we list the standard-model (see below) densities for each layer. The densities reported were obtained via a manual person driven inversion process. As the routine is not automated, ρ_{fit} of the different layers was changed and adapted until a satisfactory fit between observed Bouguer anomalies and gravity signal of the model was achieved. Figure 4 shows the gravity signal of the model as a surface and the observed Bouguer anomalies as circles. Furthermore, profiles at different *x* positions comparing observed (black symbols) and calculated Bouguer anomalies (grey lines) are plotted. The root-mean-square (RMS) error between calculated and observed Bouguer anomaly is 88 mGal.

This standard model solution represents a reasonable density distribution as it can be expected for an average lithosphere, however, it is nonunique, and many other combinations of densities can potentially yield the same gravity signal. Therefore, two additional density distributions were fitted, as listed in Table 2. They represent end-member cases: One case exhibits large-density differences between upper and lower crust but small differences between lower crust and upper lithospheric mantle. The second case exhibits large differences in density between lower crust and upper lithospheric mantle but small differences between upper and lower crust. RMS errors between calculated and observed Bouguer anomalies for these two density

Table 2. Densities Used to Calculate Bouguer Anomalies for the Model Configuration Using the Adapted Geometry[a]

Layer (Phase)	Reference Densities (kg/m^3)	Standard Model Densities (kg/m^3)	Large Difference Between Upper and Lower Crustal Densities (kg/m^3)	Large Difference Between Lower Crustal and Upper Mantle Densities (kg/m^3)
Lower lithospheric mantle (0)	3300	3300	3300	3300
Upper lithospheric mantle (1/2/5/8)	3200	3200	3200	3200
Eclogitized Indian lower crust (11)	2800	3100	3100	3100
Indian lower crust (6)	2800	2900	2950	2800
Indian upper crust (7)	2700	2675	2625	2775
Indian oceanic lower crust (9)	2800	3000	3050	2900
Indian oceanic upper crust (10)	2700	2775	2725	2875
Asian lower crust (3)	2800	2950	3000	2900
Asian upper crust (4)	2700	2850	2800	2900
Tarim and Sichuan Basins (12)	2700	2800	2800	2800
Average error (mGal)	-	87.8983	80.9697	101.3107

[a]Reference densities are based on the PREM [*Dziewonski and Anderson*, 1981]. Since the solution is nonunique, three different density profiles were fitted: (i) standard model densities, (ii) density profile with increased differences between upper and lower crustal densities, and (iii) density profile with increased differences between lower crustal and upper lithospheric mantle densities. The average point wise error (RMS error) between calculated and observed Bouguer anomaly is indicated.

distributions are 81 mGal and 101 mGal, respectively. Compared to 2-D profiles fitting Bouguer anomalies [*Hetényi et al*., 2007], where errors are usually around ± 10–20 mGal, these errors appear to be rather large (~15% of the Tibetan Plateau's signal) which we attribute to (i) the 3-D geometry of the model, (ii) the constant density of the layers, and (iii) the sparse Moho depth coverage of the Tibetan Plateau. Improved fits can

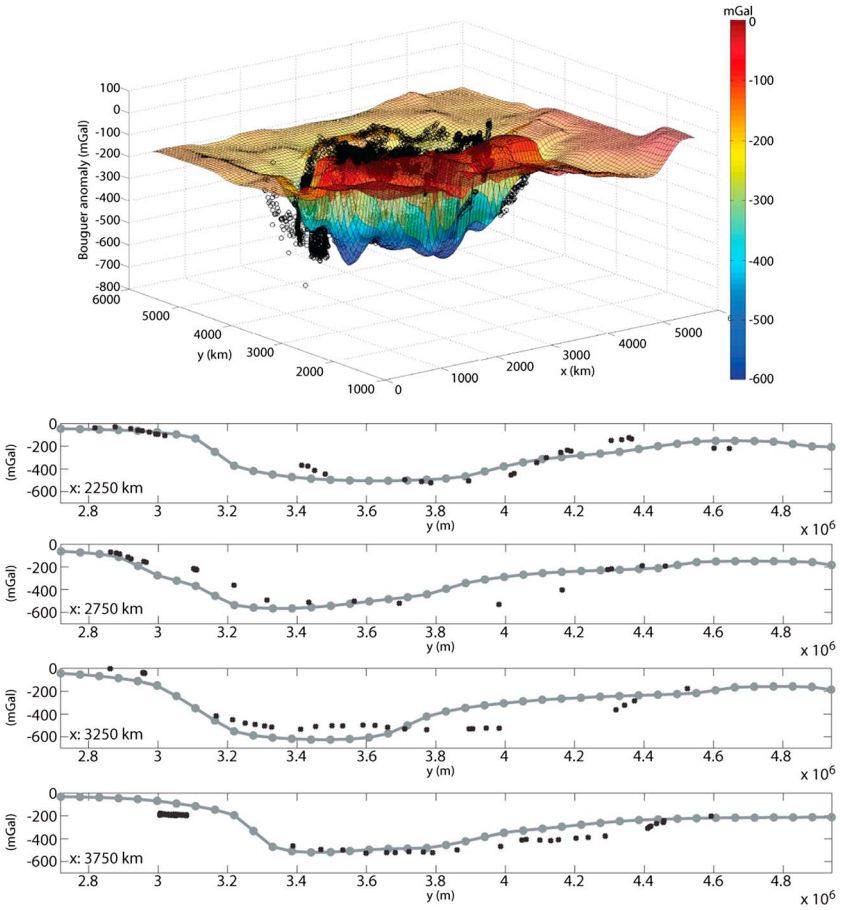

Figure 4. Bouguer anomaly (colored surface) calculated for the model setup with layer depths of the adapted geometry and using the standard model densities. For comparison also observed Bouguer anomalies are shown (black symbols) (see compilation in *Hetényi* [2007] and *Hetényi et al*. [2007]). Below, four profiles at different *x* positions (*x* = 2250, 2750, 3250, and 3750 km) are shown, comparing calculated (gray line with dots) and observed (black symbols) Bouguer anomalies within 30 km of each profile.

only be expected when Bouguer anomalies are calculated in a model with much denser geometry constraints, allowing for full 3-D variation of densities (e.g., using smaller elements with their density linked to *P-T* field and petrogenetic tables), as well as using more sophisticated and automated approaches for joint gravity and Stokes inversion. The Bouguer anomaly signal of the Tibetan Plateau is approximately −550 mGal, which corresponds to approximately 40 km thickening of the crust (from 35–40 to 75–80 km). Setting up a 3-D density model can only be done at the level corresponding to the 3-D knowledge of structures, which in the case of Tibet is quite sparse. Considering the total variation of 550 mGal for 40 km thickening, an 88 mGal misfit corresponds to a misfit of 6.4 km in modeling the thickening. This value is in the same order of magnitude as the depth definition of the Moho used in our model (see section 2.1). Therefore, with the current Moho depth information, it seems unlikely to reach better Bouguer anomaly misfits.

For the 3-D models presented here, the smallest error between the calculated gravity signal of the model and observed Bouguer anomalies was found for the density distribution with large differences in density between upper and lower crust. This is an end-member scenario with an error close to that of the standard model; therefore, these two seem to be better suited than the model with large-density contrast across the Moho. To evaluate the influence of the density distributions in more detail and to assess their impact, viscous flow simulations were performed using all three density distributions (section 3).

Studies using GPE estimates to infer magnitudes of deviatoric stresses often make use of layer depths and densities of the CRUST2.0 data set [*Ghosh et al*., 2006, 2009]. In order to estimate the improvement achieved by refining the CRUST2.0 Moho depths and constraining densities via observed Bouguer anomalies, Bouguer anomalies were also calculated for a model consisting only of CRUST2.0 data (both layer geometry and densities), resulting in a poor fit with an RMS error of 130 mGal. This clearly justifies the need to refine the CRUST2.0 geometries when working at the regional scale.

2.3. Constraining Viscosity

Viscosities in the model are temperature dependent and are calculated from experimentally derived flow laws for dry granite, diabase, mafic granulite, and wet olivine (Table 1) [*Carter and Tsenn*, 1987; *Ranalli*, 1995; *Afonso and Ranalli*, 2004; *Afonso et al*., 2007]. These flow laws are typically used for lithosphere-scale models [*Burg and Podladchikov*, 1999, 2000; *Cattin et al*., 2001; *Hetényi et al*., 2006; *Burg and Schmalholz*, 2008; *Burov*, 2010; *Hammer et al*., 2013]. The resulting depth-averaged viscosities (see section 3.4.1 and Figure 7) in the upper 100 km of the lithosphere are 10^{22} Pa s for the Tibetan Plateau and up to 10^{24} Pa s for the rest of the Asian and Indian continent. These average viscosities derived from flow laws agree with values commonly estimated for the India-Asia collision and in particular for the Tibetan Plateau [e.g., *England and Molnar*, 1997a, 1997b; *Flesch et al*., 2001].

In order to constrain viscosities and to test the viability of the chosen parameters, the GPE [e.g., *Fleitout and Froidevaux*, 1982; *Molnar and Lyon-Caen*, 1988; *Coblentz et al*., 1994; *Jones et al*., 1996] is calculated. The GPE is the potential energy arising from the density distribution of a material column and its thickness:

$$\mathrm{GPE} = \int_0^{L+h} \left(-\int_0^z \rho(z')g\,\mathrm{d}z' \right) \mathrm{d}z, \tag{2}$$

where h is the elevation, L is the isostatic compensation depth, assumed to be 100 km as in *Flesch et al*. [2001] and *Ghosh et al*. [2009], z is the vertical coordinate, ρ is the density, and g is the gravitational acceleration. A different value for L influences the resulting GPE values, although *Ghosh et al*. [2009] demonstrated that this has a minor impact on their model results. Differences in elevation and crustal thickness of a neighboring lowland and a plateau lead to lateral differences in GPE (ΔGPE). This ΔGPE is a driving force in plate tectonics; commonly observed at mid-oceanic ridges, which are elevated regions with dense mantle material below and are the origin of ridge push [e.g., *McKenzie*, 1972].

GPE and ΔGPE values were calculated numerically from the model density field, where ΔGPE was calculated by subtracting the average GPE value of the entire model from the GPE value at a specific horizontal position. GPE and ΔGPE values were calculated for the adapted CRUST2.0 geometry and the three different density distributions described in the previous section (see section 2.2 and Table 2). GPE and ΔGPE values (Figure 5a) are approximately the same for all tested density distributions. By using a compensation depth of 100 km, the calculated GPE values range between 1.25–1.5 × 10^{14} N/m and ΔGPE values between −1.5 × 10^{13} N/m and

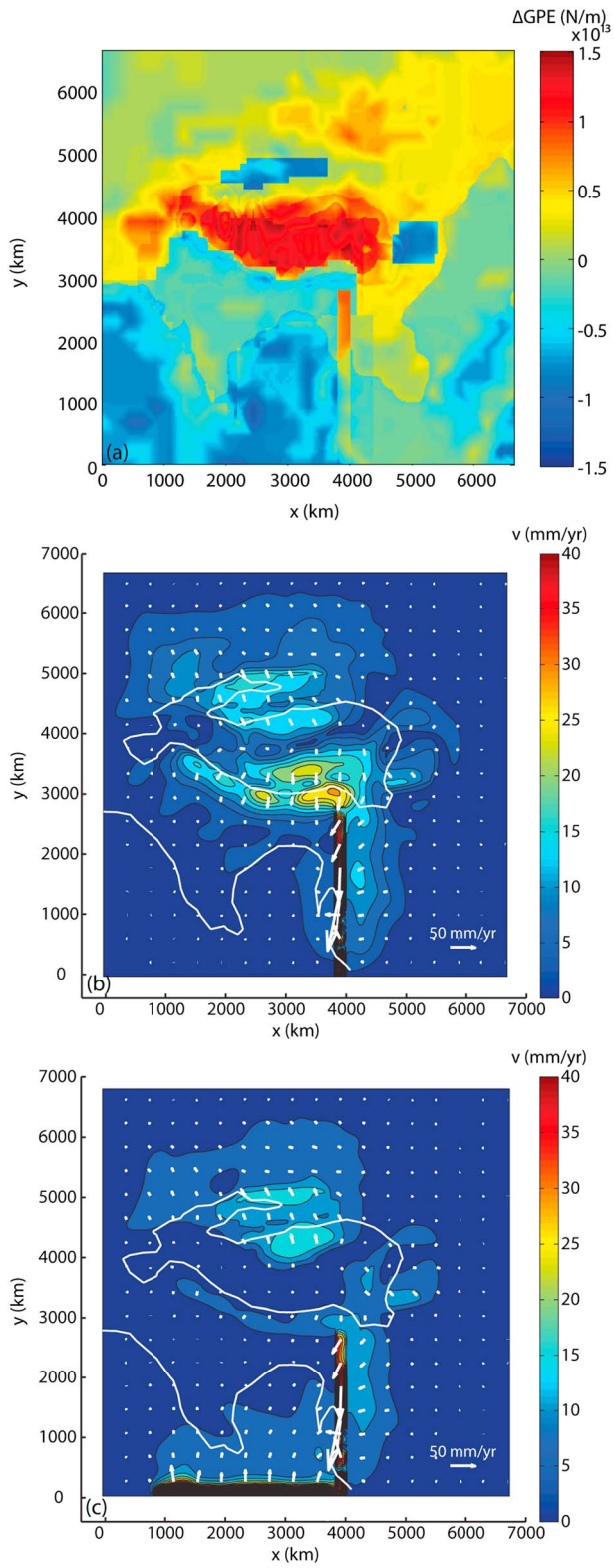

Figure 5. (a) The ΔGPE values calculated from the 3-D model using the adapted layer depths and the standard model densities described in section 2.2. (b) Colored contours and white vectors show the horizontal velocity field on the surface of the model. Due to the high GPE values in the Tibetan Plateau, horizontal velocity vectors point away from the Tibetan Plateau. Results are shown for the simulation employing the standard model densities and the viscosities derived from rheological laws, commonly used for a typical lithosphere. (c) Horizontal velocities on the surface of a model with a strong Indian lower crust (10^{24} Pa s) and a weak upper lithospheric mantle (10^{22} Pa s). Despite the indenting boundary condition (10 cm/yr), no shortening is taking place at the Himalayan front. This is due to the large velocities induced by the equilibration of lateral variations in GPE, which counteract the indentation. White contours in Figures 5b and 5c show the outlines of the Indian continent (contour line at −1 km) and the Tibetan Plateau (contour line at 1 km).

1.5×10^{13} N/m. These GPE values are within 10% of the values published by *Ghosh et al*. [2009] and are highest for the Tibetan Plateau. The rest of the Asian continent shows intermediate values, while the Indian continent and ocean along with the Tarim Basin and the Sichuan Basin show the smallest GPE values. Figure 5a shows the ΔGPE distribution with positive values for the Tibetan Plateau indicating horizontal tension, while negative ΔGPE values indicate horizontal compression.

From the distribution of the GPE it is expected that equilibrating flow is taking place from the elevated Tibetan Plateau toward the neighboring low-lying areas. However, as the Tibetan Plateau is currently in a state of ongoing south-north convergence, rather than simply collapsing, viscous stresses are sufficiently high to counteract the gravitational stresses and to support the high elevations [e.g., *England and McKenzie*, 1982; *Ellis*, 1996]. This reasoning allows us to constrain viscosities. If the employed model viscosities are too low, the lithosphere is too weak to support the large ΔGPE of the Tibetan Plateau, and flow is induced from positive to negative ΔGPE areas. An increased flow of material influences the stress, and velocity fields induced by the indentation of India into Asia and model velocities can differ significantly from measured GPS velocities. However, if viscosities are sufficiently large, viscous stresses are able to equilibrate, or overprint, gravitational stresses, and the stress and velocity fields of the modern India-Asia collisional system known from geophysical data can be reproduced.

Accordingly, the viscosity distribution, resulting from applying the rheological flow laws for dry granite, diabase, mafic granulite, and wet olivine [*Carter and Tsenn*, 1987; *Ranalli*, 1995; *Afonso and Ranalli*, 2004; *Afonso et al*., 2007] to a realistic temperature distribution for the modern India-Asia collisional system, was tested. For the scenario with no-slip lateral boundaries and only density-driven deformation (BC1), a flow pointing radially away from the Tibetan Plateau was induced with maximum surface velocities of approximately 2.5 cm/yr at the Himalayan front (Figure 5b). When applying the indenting boundary condition (BC2) at the front of the model (10 cm/yr) to the same setup, the distribution of stresses observed for the modern India-Asia orogen [e.g., *Armijo et al*., 1986; *Taylor et al*., 2003; *Heidbach et al*., 2008], and the surface velocity field can be reproduced more or less correctly (see section 4.1.1 and Figure 12). However, for other viscosity distributions, for example, when increasing the viscosity of the Indian lower crust to a constant value of 10^{24} Pa s and decreasing the viscosity of the Indian upper lithospheric mantle to a constant value of 10^{22} Pa s, the flow induced by the distribution of ΔGPE away from the Tibetan Plateau is much larger. The indenting boundary condition is not able to balance or counteract this flow (Figure 5c). A much higher indenting velocity would be required to counteract the velocity field induced by the variations of GPE, in disagreement with observational constraints, which leads us to conclude that this viscosity distribution is unlikely.

The viscosity distribution resulting from a typical temperature distribution together with typical flow laws for lithospheric rocks is therefore a good first approximation (see section 3.4.1 and Figure 7). In order to develop better constraints on viscosity, we investigate in the following sections the impact of individual model assumptions and material parameters in more detail.

3. Simulations

3.1. Introduction

We performed many simulations to test the impact of different model parameters on the results. First, we present representative results for the 3-D distribution of the pressure that is a key parameter controlling viscous flow in our mechanically layered 3-D model. Next, we summarize the impact of varying the density that is a parameter without significant impact on the model results. Finally, we present results for different values of the thickness of the lower crust and for different values of the viscosities of the weak fault zones and of the Indian lower crust, which are all model parameters that have a significant impact on the results.

3.2. Pressure

The pressure, p, is defined here in a standard fluid mechanics way as the negative mean stress (see Appendix A; also e.g., *Batchelor* [1967]). Lateral differences in the GPE result in variations of stresses [e.g., *Molnar and Lyon-Caen*, 1988; *Ghosh et al*., 2006]. Stresses resulting from GPE variations have been investigated mainly with thin-sheet models [*Ghosh et al*., 2006, 2009], but the pressure variations resulting from GPE variations have attracted less attention. The impact of the GPE distribution on the pressure field is illustrated in Figure 6 where the difference ($P_{\mathrm{diff}} = p - P_{\mathrm{litho}}$) between pressure, i.e., the pressure resulting from solving the Stokes

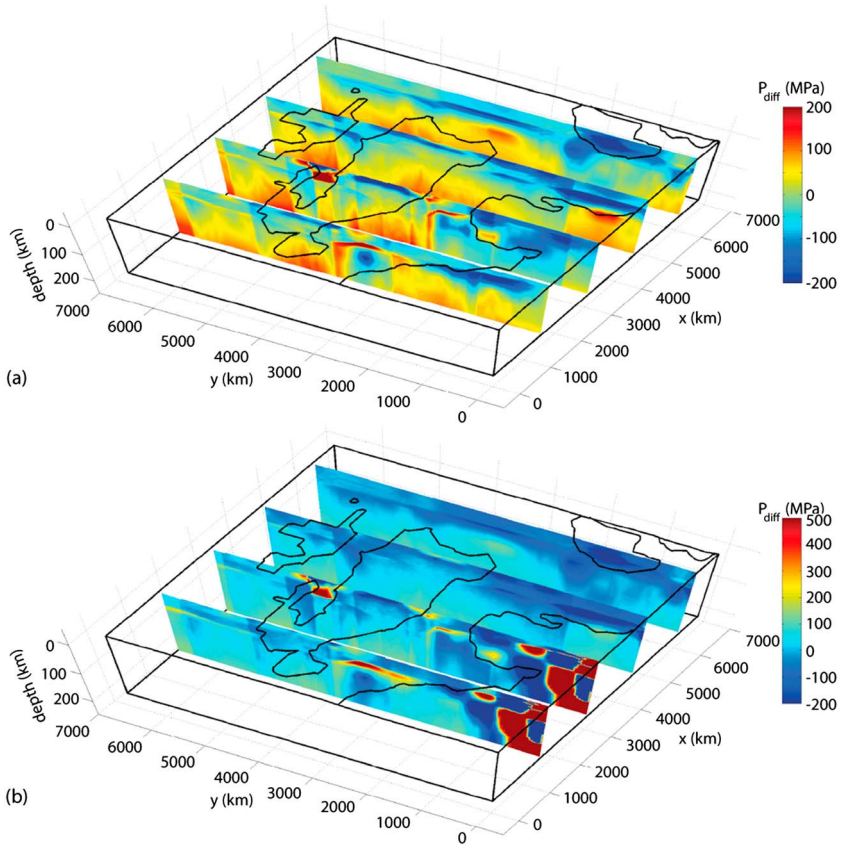

Figure 6. Difference between pressure and lithostatic pressure ($P_{diff} = p - P_{litho}$) of simulations (a) with only gravity as the driving force and (b) with the indenting boundary condition, employing the standard model densities and the viscosities derived from flow laws commonly used for a typical lithosphere. Black contours on the surface of the surrounding model box show the outlines of the Indian continent (contour line at −1 km) and the Tibetan Plateau (contour line at 1 km). In Figure 6a pressure is larger than lithostatic pressure below the Tibetan Plateau due to stresses induced by the lateral variations in GPE. The maximum values in the Indian lower crust are about 500 MPa. In Figure 6b pressure is also larger than the lithostatic pressure at the model front, where boundary conditions are applied. The pressure difference is also larger in the underthrusting Indian lower crust (~ 800 MPa).

equation (Appendix A, equation (A6)), and lithostatic pressure (P_{litho}, resulting only from the vertical integral of the density distribution) is shown. The pressure difference P_{diff} is often termed tectonic pressure or tectonic overpressure [e.g., *Petrini and Podladchikov*, 2000; *Mancktelow*, 2008; *Schmalholz and Podladchikov*, 2013]. The tectonic pressure field in Figure 6a results from a density-driven simulation. For comparison, in Figure 6b the tectonic pressure is shown for a simulation where in addition to variations in GPE also the indenting boundary condition was used (see section 2.1). In Figure 6a lateral variations in GPE induce an equilibrating flow, smoothing out differences in topography and crustal thickness. This flow is most pronounced below the Tibetan Plateau and can also be observed in Figure 6a from the elevated values of P_{diff} of 100–150 MPa below the Tibetan Plateau, where positive values indicate larger pressure, i.e., tectonic overpressure. Away from the Tibetan Plateau tectonic pressure is much smaller and even tends toward zero in the east of the Tibetan Plateau. Locally in the underthrusting Indian lower crust, tectonic pressure can exceed 200 MPa. The tectonic pressure is due to the horizontal force per unit length that is caused by variations in GPE between a neighboring lowland and mountain [e.g., *Molnar and Lyon-Caen*, 1988]. Tectonic pressures vary vertically and are higher in mechanically stronger layers and also in the upper and colder part of the lithosphere due to the temperature dependence of the viscosity and the related vertical variation of deviatoric stresses. The simulations driven by density and with an indenting boundary velocity show a similar pattern for P_{diff} below the Tibetan Plateau. However, the two simulations differ in the underthrusting Indian lower crust which exhibits a larger, maximal tectonic overpressure in Figure 6b (~800 MPa) than in Figure 6a (~500 MPa). This is in agreement with GPE values and is explained by the mechanical layering of the lithosphere. Different layers compensate different amounts of lateral GPE variations depending on their strength: mechanically resistant

(and colder) areas hold most of the horizontal force per unit length resulting from GPE variations and are therefore under higher stress. The 3-D model can be used to quantify magnitudes and distributions of forces, stresses, and pressure resulting only from static gravitational stresses (Figure 6a) and from dynamic tectonic forces (Figure 6b) for the modern India-Asia collisional system.

Stresses and tectonic pressure at the southern edge of the model are affected by the indenting boundary conditions, and stresses and tectonic pressure inside the effectively rigid basins are affected by the assumption of effective rigidity. We focus here only on the pressure in the underthrusting Indian lower crust. The maximal tectonic overpressure of ~800 MPa occurs in the Indian lower crust in a depth of approximately 70 km for the indenting scenario. Assuming an average density of 2800 kg m^{-3}, the lithostatic pressure in 70 km depth is approximately 2.1 GPa (including 5 km topography). Therefore, the tectonic overpressure in the Indian lower crust is less than half of the corresponding lithostatic pressure (approximately 38% of the lithostatic pressure). Analytical and numerical studies have shown that for a friction angle of 30°, the tectonic overpressure corresponds to approximately the lithostatic pressure [e.g., *Petrini and Podladchikov*, 2000]. Therefore, the tectonic overpressure of 800 MPa is consistent with the theoretical frictional strength of rocks. Furthermore, analytical and numerical studies show that in viscous materials, the tectonic overpressure is usually of the same magnitude as the deviatoric stress [e.g., *Mancktelow*, 2008, and references therein]. Recent experimental studies combined with micromechanically motivated flow laws show that the stress in lower crustal rocks (omphacite) is approximately 1 GPa for a temperature of 500°C and for tectonically realistic strain rates between 10^{-13} and 10^{-15} s^{-1} [e.g., *Moghadam et al*., 2010]. The maximal differential stress (i.e., square root of second invariant of deviatoric stress tensor) in the Indian lower crust in our model is less than 1 GPa, and therefore, the numerically calculated stresses in the strong Indian lower crust are compatible with stress estimates for lower crustal rocks. The numerically determined tectonic overpressure in the strong Indian lower crust is, therefore, mechanically plausible, and the corresponding stress magnitudes are compatible with stress predictions from experimental studies.

3.3. Model Parameter Without Significant Impact—Density Distribution

Determination of densities by fitting the Bouguer anomalies is nonunique. Therefore, three different possible density distributions were constructed namely one standard and two end-member distributions (see section 2.2 and Table 2). (1) The standard model density distribution consists of values representing an undeformed lithosphere with a standard geotherm. (2) A second density distribution exhibits large differences (200–325 kg/m^3) between the upper and lower crust but small differences (100–250 kg/m^3) between the lower crust and upper lithospheric mantle. (3) The third density distribution shows large differences (300–400 kg/m^3) between lower crust and upper lithospheric mantle and small differences (~25 kg/m^3) between upper and lower crust. With these three density distributions, we performed simulations for both boundary conditions. Except for density, all other material parameters were identical in all simulations.

The resulting GPE variations for the three density distributions are very similar, which is why there are virtually no differences between the simulations with only density-driven deformation or prescribed indenting boundary velocities. Due to the identical viscosity distribution in all models, no differences can be seen in the stress, pressure, and strain rate fields. Minimal differences only can be identified in the horizontal and vertical velocity fields in the area of the Tarim Basin and the Sichuan Basin. However, the model kinematics is not significantly influenced by the three different density distributions. Therefore, for all subsequent simulations the standard model density distribution was employed.

3.4. Model Parameters With Significant Impact

3.4.1. Thickness of Lower Crust

In the standard model configuration the upper crust is composed of the upper and middle crust of the CRUST2.0 data set. This geometry was used for all simulations discussed in section 3.4. In order to assess the impact of a different distribution of thicknesses in the crust, a simulation was also performed with the middle and lower crust of CRUST2.0 composing the lower crust of the model (Figure 7). The temperature distribution of the model with a thin lower crust has high temperatures below the Tibetan Plateau and lower temperatures below the Indian continent (Figures 7b and 7c). The geotherm of the Indian continent (Figure 7c) approximately corresponds to the steady state geotherm of the South Indian Shield suggested by *Priestley et al*. [2008] that was constrained with xenolith data. A thicker lower crust results in lower temperatures below the Tibetan Plateau (Figures 7e and 7f) because the crustal layer with lower radioactive heat production defines

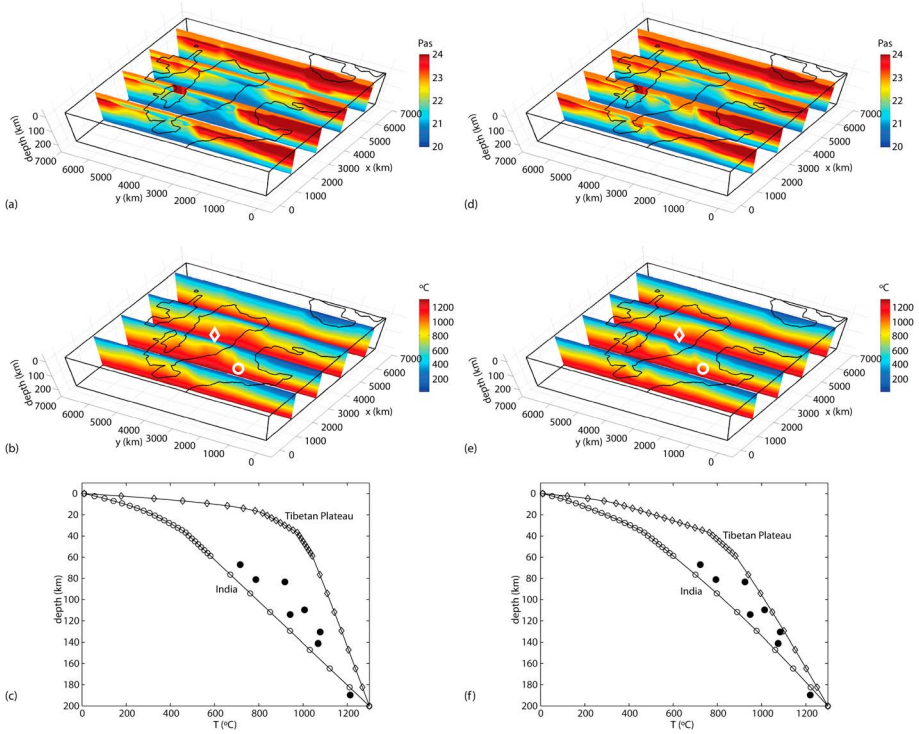

Figure 7. Comparison of simulations with (a–c) a thin and (d–f) a thick lower crust, using the standard model densities and the viscosities derived from flow laws commonly used for a typical lithosphere. Figures 7a and 7d show the logarithm of the viscosity distribution, and Figures 7b and 7e show the 3-D temperature field. Black contours on the surface of the surrounding model box show the outlines of the Indian continent (contour line at −1 km) and the Tibetan Plateau (contour line at 1 km). Figures 7c and 7f show model geotherms for India and the Tibetan Plateau (exact locations are shown in Figures 7b and 7e). Furthermore, upper mantle xenolith data (filled circles) of *Priestley et al.* [2008] are shown. A larger thickness of the lower crust leads to lower temperatures and higher viscosities below the Tibetan Plateau.

the major part of the crust. This causes viscosities to be higher and therefore the crust to be generally stiffer (Figure 7d). As a result, this leads to a more uniform vertical distribution of viscosities. Consequently, the horizontal velocity field does also not show significant differences between the different layers. Horizontal velocities in the crustal layers are slightly increased in the model exhibiting a thick lower crust. Strain rates are smaller by approximately 1 order of magnitude in all layers below the Tibetan Plateau in the model with a thick lower crust compared to the equivalent model with a thin lower crust. Stresses differ by less than 200 MPa between models with a thick and a thin lower crust. In the model with a thick lower crust, stresses in the upper lithospheric mantle are larger (by 300–400 MPa) than in the model with a thin lower crust. This is due to the lower temperatures at depth in the model with a thick lower crust, thus leading to a stiffer upper lithospheric mantle.

The relative thickness of different layers has a considerable impact on the model results because the layer thickness controls the vertical temperature variations, which in turn modifies the vertical viscosity variation (Figure 7). For the following simulations, we used the option with upper and middle crust of CRUST2.0 composing the upper crust of the model (i.e., the hotter model). In section 4 we discuss the need for a better distinction of the layers.

3.4.2. Viscosity of Weak Zones

The Quetta-Chaman Fault and the Sagaing Fault were assigned a constant viscosity of 10^{20} Pa s in the standard model. In order to assess the impact of the viscosity of these weak zones, simulations were performed with constant viscosities of 10^{18} Pa s and 10^{22} Pa s. Simulations in which a viscosity of 1018 Pa s was employed had very large velocities in the weak zone which in turn resulted in a large grid deformation within 2500 years. Strain rates are smaller by half an order of magnitude in the weak zones with a viscosity of 10^{22} Pa s compared to weak zones with a viscosity of 10^{20} Pa s. However, strain rates in the rest of the model domain are unaffected by the viscosity of the weak zones. Stresses also only differ slightly at the location of the faults for the different viscosities. The choice of weak zone viscosity, however, has an

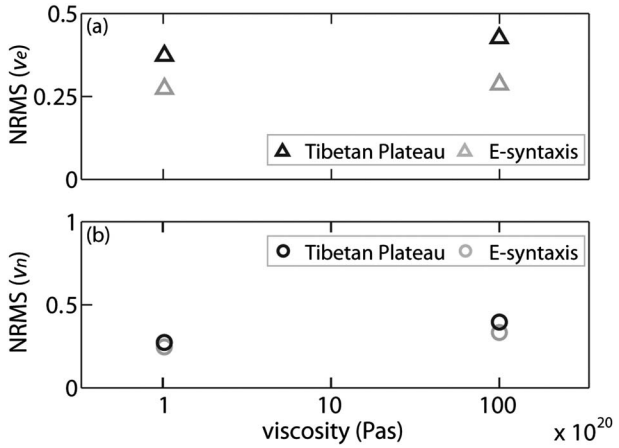

Figure 8. Normalized root-mean-square (NRMS) error between model and GPS velocities for viscosities (10^{20} Pa s and 10^{22} Pa s) of the weak zones, representing the Quetta-Chaman and the Sagaing Faults. (a) The east directed velocity component (v_e) for the Tibetan Plateau (black) and the area around the eastern syntaxis (grey). (b) The north directed velocity component (v_n) for the Tibetan Plateau (black) and the area around the eastern syntaxis (gray).

important impact on the horizontal velocity field. A viscosity of 10^{22} Pa s leads to a decreased west directed flow in the area of the Quetta-Chaman Fault in the west and a better fit of observed GPS velocity directions in the western half of the Tibetan Plateau. Velocities around the eastern syntaxis are increased by 1–2 cm/yr. Furthermore, the area east of the Sagaing Fault is moving northward, leading to velocity vectors pointing in the opposite direction of GPS velocities. Normalized root-mean-square (NRMS) errors between

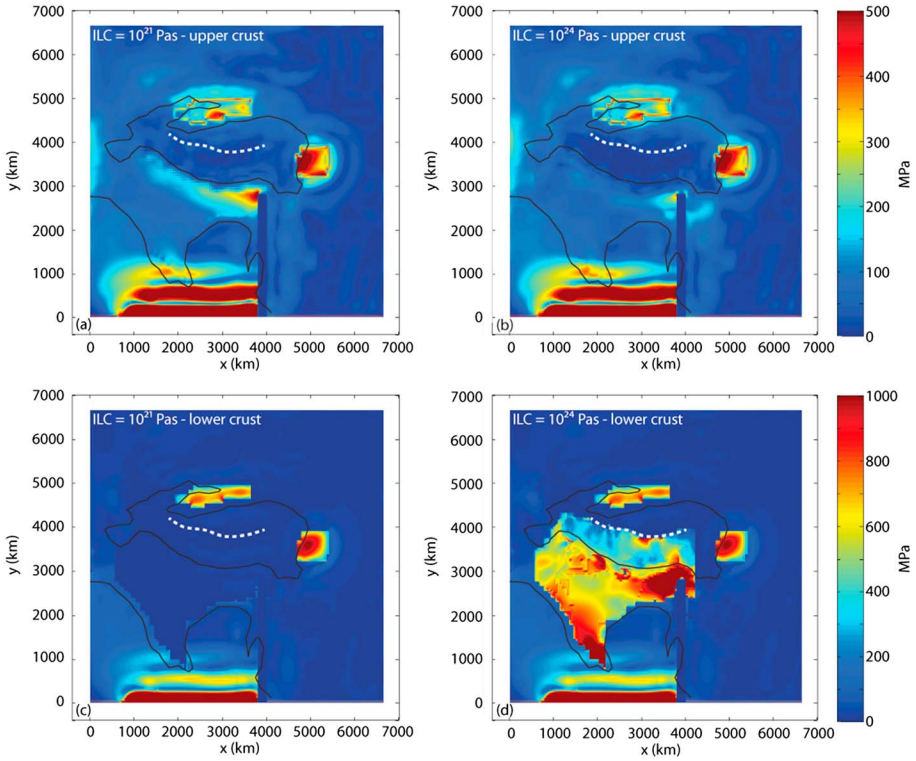

Figure 9. Square root of the second invariant of the stress tensor for (a, c) the model exhibiting an Indian lower crustal (ILC) viscosity of 10^{21} Pa s and (b, d) the model exhibiting an Indian lower crustal viscosity of 10^{24} Pa s. Figures 9a and 9b show stresses in the upper crust, and Figures 9c and 9d show stresses in the lower crust. The black lines indicate the outlines of the Tibetan Plateau (contour line at 1 km) and the Indian continent (contour line at −1 km). The white-dashed line represents the northern boundary of the underthrusting Indian lower crust.

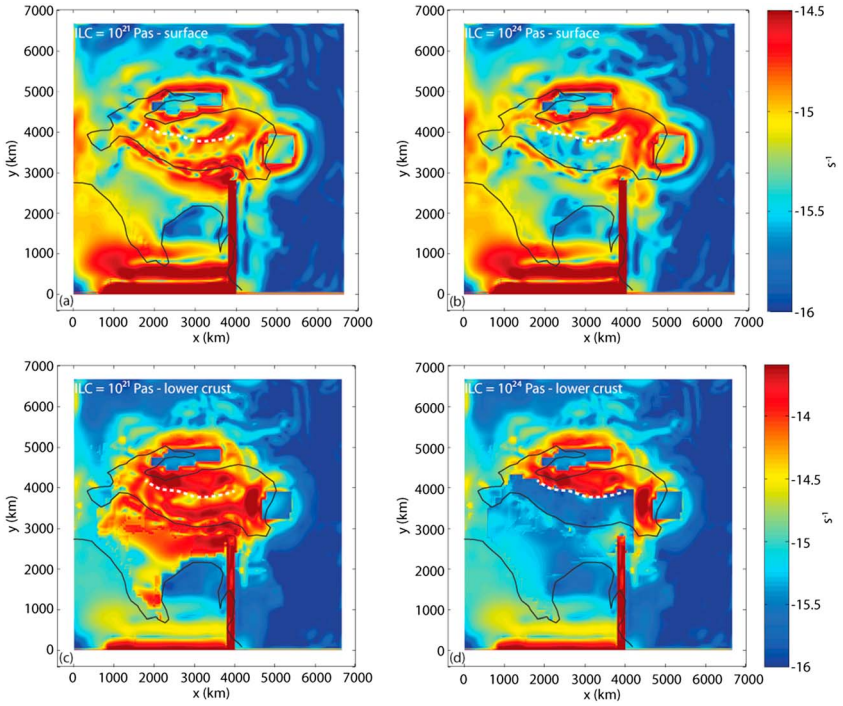

Figure 10. Color plot of the logarithm of the square root of the second invariant of the strain rate tensor for (a, c) the model exhibiting an Indian lower crustal (ILC) viscosity of 10^{21} Pa s and (b, d) the model exhibiting an ILC viscosity of 10^{24} Pa s. Figures 10a and 10b show strain rates on the surface, and Figures 10c and 10d show strain rates in the lower crust. The black lines indicate the outlines of the Tibetan Plateau (contour line at 1 km) and the Indian continent (contour line at −1 km). The white-dashed line represents the northern boundary of the underthrusting Indian lower crust.

model and GPS velocities are smaller when applying a viscosity of 10^{20} Pa s for the weak zones instead of 10^{22} Pa s (Figure 8). For a viscosity of 10^{20} Pa s the NRMS error for the area around the eastern syntaxis is 0.26 for the east directed velocity component (v_e, Figure 8a) and 0.24 for the north directed component (v_n, Figure 8b). For the entire plateau a velocity misfit $v_e = 0.35$ and $v_n = 0.26$ is observed. For a viscosity of 10^{22} Pa s the misfit for the area around the eastern syntaxis is 0.27 for v_e and 0.32 for v_n. For the Tibetan Plateau the NRMS error is 0.42 for v_e and 0.39 for v_n. GPS velocities around the eastern syntaxis can only be fitted well with a viscosity of 10^{20} Pa s for the Sagaing Fault (see section 4.1.1). Thus, 10^{22} Pa s is the preferred viscosity for the Quetta-Chaman Fault in the west and 10^{20} Pa s for the Sagaing Fault in the east (see sections 4.1.1 and 4).

3.4.3. Viscosities of the Lower Crust and Upper Lithospheric Mantle

The viscosity of the Indian lower crust and upper lithospheric mantle were varied to study their impact on the stress and strain rate fields within the different layers. In a first set of simulations, the viscosity of the Indian lower crust was varied (assuming constant values throughout the layer) between 10^{21} and10^{24} Pa s. Results show that with increasing viscosity stresses within the Indian lower crust increase (locally $>$ 1000 MPa), whereas the rest of the model remains largely unaffected (Figures 9c and 9d). For a variation of 3 orders of magnitude in viscosity, stresses vary by approximately 2 orders of magnitude. The Indian lower crustal viscosity, however, not only affects its own stress level but also that of the upper crust (Figures 9a and 9b). Compared to a model with a competent Indian lower crust (10^{24} Pa s), stresses in the upper crust above a relatively weak Indian lower crust (10^{21} Pa s) are increased by only a few 100 MPa at the eastern syntaxis and south of the Tibetan Plateau, where the Main Frontal Thrust and the Main Boundary Thrust [e.g., *Meigs et al.*, 1995] of the Himalaya are situated (Figure 9a).

On the other hand, strain rates in the Indian lower crust decrease with increasing viscosity (Figures 10c and 10d). In the portion of the lower crust, underthrusting the Tibetan Plateau differences between strain rates in a competent lower crust (10^{24} Pa s) and a relatively weak lower crust (10^{21} Pa s) are approximately 2 orders of magnitude. However, when varying the Indian lower crustal viscosity by 3 orders of magnitude, differences

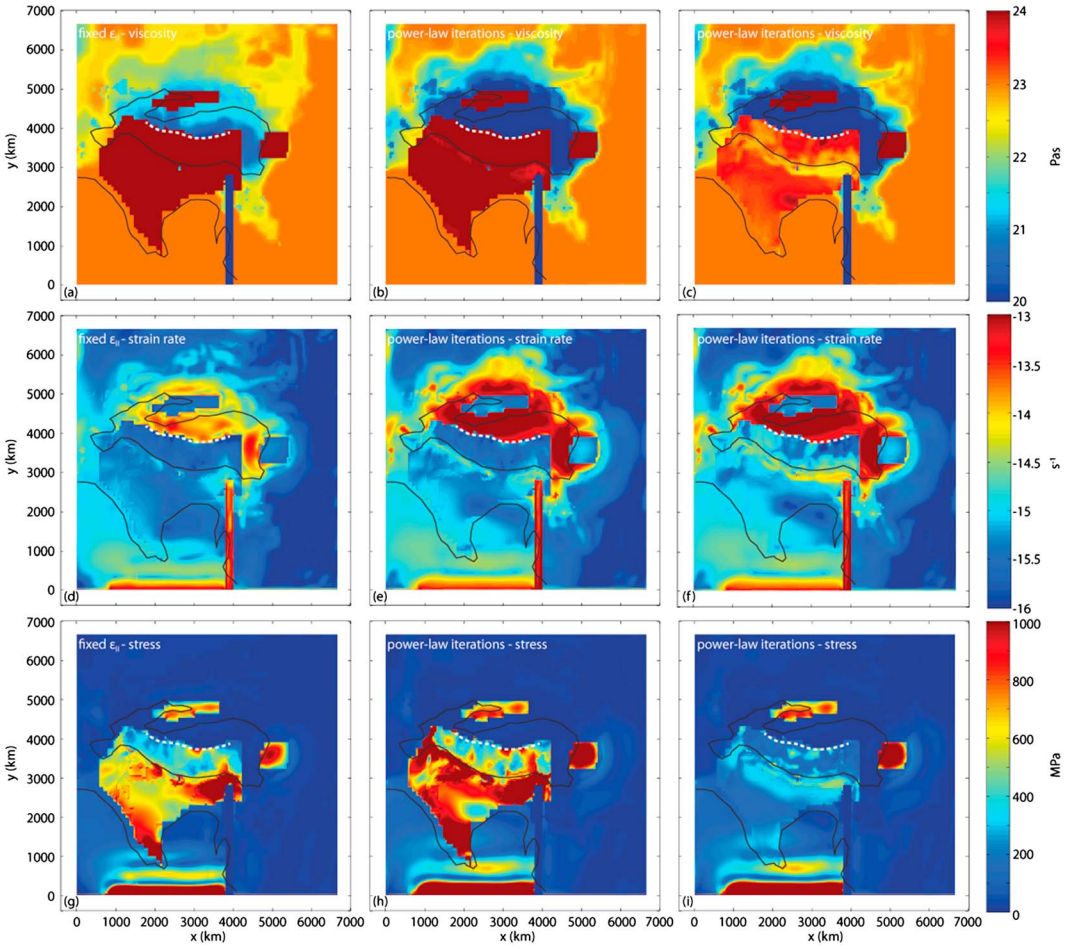

Figure 11. Comparison of simulations using (a, d, g) a fixed value for the square root of the second invariant of the strain rate tensor, $\dot{\varepsilon}_{II}$ (= 10^{-15} s^{-1}), (b, e, h) employing four power law iterations for an effective Indian lower crustal viscosity of 10^{24} Pa s, and (c, f, i) employing four power law iterations for an effectively power law viscous Indian lower crust. Figures 11a–11c denote logarithm of effective viscosity. Figures 11d–11f show logarithm of $\dot{\varepsilon}_{II}$. Figures 11g–11i show square root of the second invariant of the stress tensor. The black lines indicate the outlines of the Tibetan Plateau (contour line at 1 km) and the Indian continent (contour line at −1 km). The white-dashed line represents the northern boundary of the underthrusting Indian lower crust.

between strain rates on the surface are less than 1 order of magnitude (Figures 10a and 10b). North of the underthrusting Indian lower crust and east of the Sichuan Basin, strain rates of both the upper and lower crust do not differ for the different viscosities applied. In addition, the velocity field is affected by the choice of the Indian lower crustal viscosity. Velocities of the layers above and below increase with increasing Indian lower crustal viscosity (1–2 cm/yr). Differences in magnitude and direction of the velocity field between the different layers decrease with increasing viscosity.

The Indian upper lithospheric mantle also has an important influence on the model kinematics. The standard model has a viscosity of approximately 10^{24} Pa s, whereas it was varied for constant values from 10^{22} Pa s to 10^{25} Pa s in a series of simulations. With a viscosity as low as 10^{22} Pa s, model results deviate strongly from the standard model results. The influence of the velocity field induced by the lateral variations of GPE is larger than the indenting boundary condition, and thus, unrealistic results are produced (see section 2.3). A large viscosity such as 10^{25} Pa s on the other hand results in unrealistically high velocities in the entire model for the employed boundary conditions. This is due to the very stiff character of the upper lithospheric mantle which is translated by the boundary conditions as a rigid block into the model, dragging along the layers above and below, which do not exhibit any variations in the stress, strain rate, and velocity fields anymore. The most realistic model results were achieved when employing an Indian lower crustal viscosity of 10^{21}–10^{24} Pa s and an Indian upper lithospheric mantle viscosity of 10^{24} Pa s.

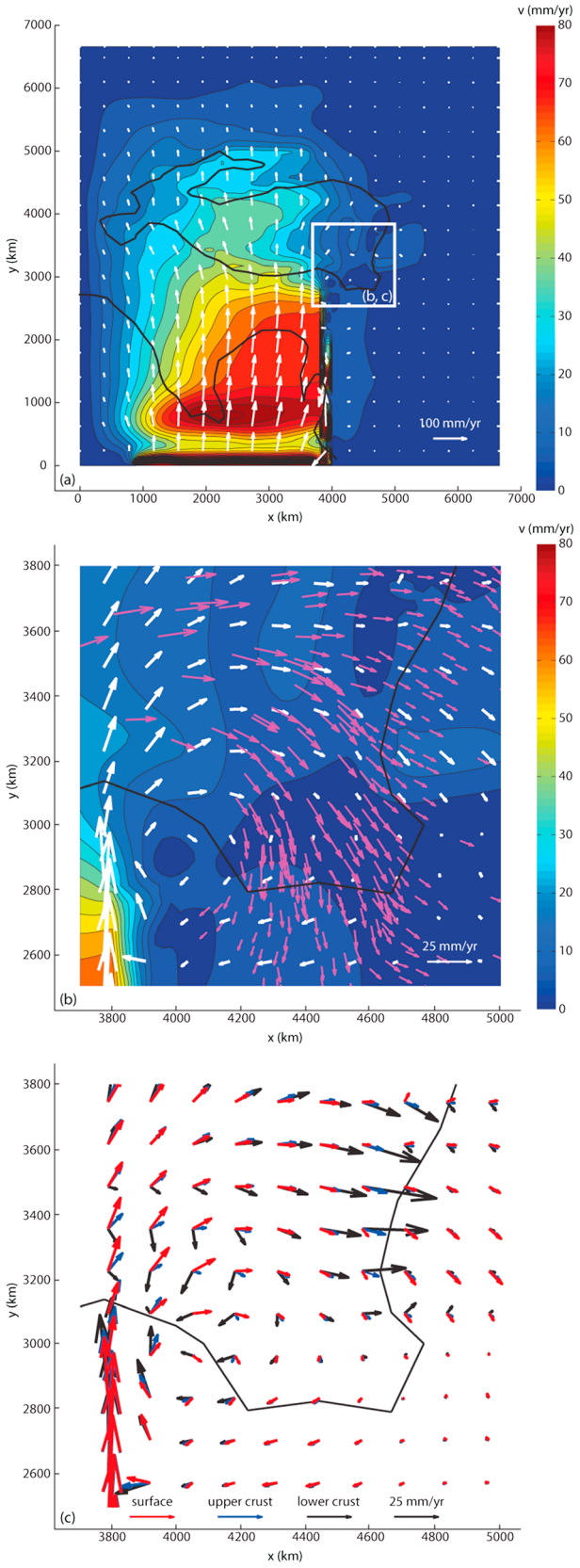

Figure 12

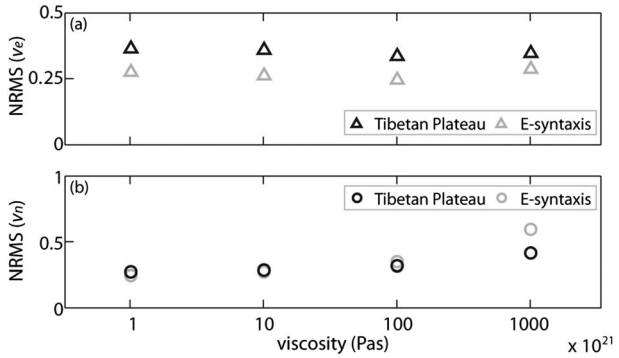

Figure 13. Normalized root-mean-square (NRMS) error between model and GPS velocities for viscosities (10^{21}–10^{24} Pa s) of the underthrusting Indian lower crust. (a) The east directed velocity component (v_e) for the Tibetan Plateau (black) and the area around the eastern syntaxis (gray). (b) The north directed velocity component (v_n) for the Tibetan Plateau (black) and the area around the eastern syntaxis (gray).

The reported results used a simplified temperature-dependent rheology, with a fixed square root of the second invariant of the strain rate tensor $\left(\dot{\varepsilon}_{II} = 10^{-15}\mathrm{s}^{-1}\right)$ to save computational resources. The simulations with an Indian lower crustal viscosity of 10^{21} and 10^{24} Pa s, however, were also performed without a constant value of $\dot{\varepsilon}_{II}$ but instead performing four nonlinear iterations per time step. At this point, the error of two subsequent solutions for the velocity field was approximately 0.01. In two simulations the effective viscosity of the Indian lower crust was fixed at 10^{21} and 10^{24} Pa s (Figure 11b), respectively. This implies that the effect of performing power law iterations can only be observed in the adjacent layers. Results show that the patterns and the relative distribution of velocities, strain rates, and stresses remain the same (Figures 11d, 11e, 11g, and 11h). However, the absolute values of the aforementioned quantities do change, as expected. As a result of increased strain rates the effective viscosity of the Asian lower crust below the Tibetan Plateau is decreased by 1–1.5 orders of magnitude when using power law iterations (Figure 11b). Strain rates show slightly larger values (by a factor of 3) in the Indian lower crust (Figure 11e). The increased strain rates and the fixing of the effective viscosity of the Indian lower crust at 10^{24} Pa s causes its stresses to be higher. Accounting also for the power law effect in the Indian lower crust results in decreased effective viscosities (Figure 11c, 1–1.5 orders of magnitude). Compared to the simulation with a fixed effective Indian lower crustal viscosity, strain rates are further increased in the underthrusting part of the crust and at the front of the Himalaya (Figure 11f). Stresses in the Indian lower crust are decreased by several 100 MPa due to the decreased viscosities (Figure 11i). Thus, depending on the applied flow law, results differ in their absolute values, while the relative pattern remains similar. More realistic and accurate results, including the strain rate dependence of the viscosity, can be achieved when also performing power law iterations.

4. Discussion

4.1. Comparison of Model Results With Measured Data and Geological Observations

4.1.1. Comparison of the Horizontal Velocity Field on the Surface With GPS Data

GPS velocities can be used to test the robustness of the model configuration by comparing them to the horizontal velocities on the surface of the model. Figure 12a shows the horizontal velocities on the surface of the model (white arrows and colored contours), including the boundary velocities (i.e., 10 cm/yr). In Figure 12b a zoomed-in image of the eastern syntaxis is shown with measured GPS data (Figure 12b, magenta) [*Gan et al*., 2007]. Similar fits between model and GPS velocities are obtained with viscosities of 10^{21}–10^{24} Pa s for the Indian lower crust and a viscosity of 10^{24} Pa s for the Indian upper lithospheric mantle. NRMS errors for these viscosity distributions range between 0.30 and 0.35 for v_e (Figure 13a) and between 0.26 and 0.32 for v_n (Figure 13b) for the area of the Tibetan Plateau. Velocities in the area of the eastern syntaxis yield a better fit with NRMS values between 0.24 and 0.26 for v_e (Figure 13a) and NRMS values between 0.24 and 0.36

Figure 12. Horizontal velocities of the model with an Indian lower crustal viscosity of 10^{22} Pa s and from GPS data, with respect to stable Eurasia. (a) Colored contours and white vectors show the horizontal velocity field on the surface of the model. (b) Zoomed-in image of the eastern syntaxis with GPS data of *Gan et al*. [2007] in magenta for comparison. (c) Zoom of the eastern syntaxis with horizontal velocities in different model layers: surface = red, upper crust = blue, and lower crust = black. Black contours represent the outlines of India (contour line at −1 km) and the Tibetan Plateau (contour line at 1 km).

for v_n (Figure 13b). The larger misfit for north directed velocities in the area of the eastern syntaxis for an Indian lower crustal viscosity of 10^{24} Pa s is due to increased northward flow of surface material. Misfits in this study expressed in terms of RMS for the Tibetan Plateau are around 10 mm/yr for v_e and 16 mm/yr for v_n. RMS errors in the area of the eastern syntaxis range between 4 and 7 mm/yr for v_e and between 8 and 15 mm/yr for v_n. Compared to other studies these errors seem large: *Wang et al*. [2008b] tested frictional coefficients of large-scale faults in and around the Tibetan Plateau and reached RMS errors between model and GPS velocities of 4 and 4.8 mm/yr. However, especially around the eastern syntaxis, in the Sichuan-Yunnan area, their model velocities have a poor fit with observed GPS velocities. *Copley and McKenzie* [2007] have tested various combinations of crustal densities and viscosities to model crustal flow in Tibet and found a best fit model for the eastern plateau using a crustal viscosity of 10^{22} Pa s with an error of 2 mm/yr. However, model and GPS velocities were only compared along a single profile, while here RMS misfits are calculated for large areas. Fits in this study are improved if only the Sagaing Fault is included as a weak zone (10^{20} Pa s). Including also the Quetta-Chaman Fault resulted in a stronger westward movement in the western parts of India. The results for different strengths of the two fault zones and the findings of section 3.4.2 suggest that the Quetta-Chaman Fault is mechanically stronger or accommodates less motion than the Sagaing Fault. The weak zone in the model representing the Sagaing Fault is necessary in order to produce the distinct clockwise rotation around the eastern syntaxis (Figure 12b).

Figure 12c represents the horizontal velocity fields at different model depths (surface, upper crust, and lower crust) around the eastern syntaxis. Flow directions and magnitudes in the different layers show large differences. Flow in the lower crust is strongest west of the Sichuan Basin, while in the basin itself velocities in the lower crust tend to zero.

The weak zones, representing the Quetta-Chaman Fault and the Sagaing Fault, influence the surface velocities significantly. While the Sagaing Fault appears to be weak (10^{20} Pa s) and a prerequisite to generate the clockwise rotation around the eastern syntaxis, the Quetta-Chaman Fault seems to be stronger (10^{22} Pa s) or accommodates less motion. These results agree with studies stating that the Quetta-Chaman Fault experiences low to moderate activity [*Quittmeyer and Jacob*, 1979; *Szeliga et al*., 2012] and that the Sagaing Fault accommodates most motion of India past Indochina [*Le Dain et al*., 1984; *Michel et al*., 2000; *Meade*, 2007]. The Quetta-Chaman Fault and the Sagaing Fault were included in the model as the GPS velocity field could be fitted only with these weak zones. Small NRMS misfits are achieved for the area of the eastern syntaxis with a viscosity of 10^{20} Pa s for the Sagaing Fault. Nonetheless, fits of model and GPS velocities still can be improved by, for example, testing different boundary conditions, such as applying a constant indenting velocity at the base of the Indian continent, or by comparing the impact of a deformable versus a rigid Indian indenter. For future studies also the impact of other major faults, such as the Karakorum, the Altyn Tagh, or the Red River Faults, should be investigated.

4.1.2. Deviatoric Stress Field

Surface fault orientations, which are young features of the India-Asia collision system [*Armijo et al*., 1986], can be compared with modeled stress fields. Figure 14 shows the horizontal principal stresses, i.e., the eigenvalues and eigenvectors, of the deviatoric stress tensor on the surface (Figure 14a), in the middle of the upper (Figure 14b) and lower crust (Figure 14c). Black vectors represent extensional stresses, and light grey vectors represent compressional stresses. Very large vectors at the front of the model related to the boundary conditions have been omitted on the plots for better visibility. Results are reported for the simulation with an Indian lower crustal viscosity of 10^{23} Pa s, an Indian upper lithospheric mantle viscosity of 10^{24} Pa s, and a model geometry that only includes the Sagaing Fault.

On the surface (Figure 14a) the approximately north-south directed compression of India is indicated by the orientation of the principal stresses. Compressive stress orientations largely agree with thrust fault locations of the World Stress Map of the area [*Heidbach et al*., 2008]. These compressional stresses are accompanied by smaller east-west directed extensional stresses. East-west extension is more dominant on the Tibetan Plateau, where north-south trending normal faults [*Armijo et al*., 1986; *Taylor et al*., 2003; *Heidbach et al*., 2008] are observed in nature. The Tarim Basin and the Sichuan Basin are dominated by northwest-southeast directed extension. Stresses in the basins are large due to their high viscosity (10^{24} Pa s). Our model also shows that stress orientations and horizontal velocities change direction around the eastern syntaxis.

Stress distributions in the upper crust (Figure 14b) are similar to those at the surface although stresses in the Tibetan Plateau, the Tarim Basin and the Sichuan Basin are much smaller. This can be accounted to the lower

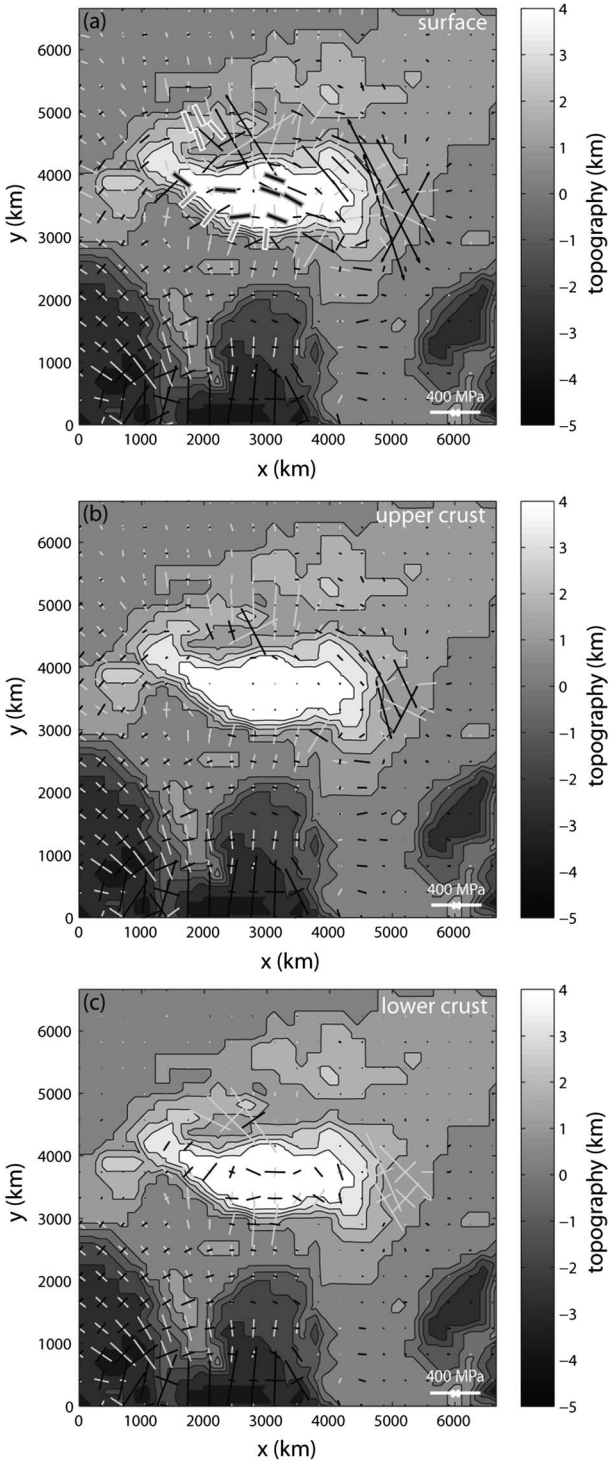

Figure 14. Horizontal deviatoric stresses of the model with an Indian lower crustal viscosity of 10^{23} Pa s (a) on the surface, (b) in the upper crust, and (c) in the lower crust. Black vectors indicate extensional stresses; light grey vectors represent compressional stresses. Colored contours show the topography of the surface. In Figure 14a the thick bars represent selected data from the World Stress Map [*Heidbach et al.*, 2008] for comparison. The bars exhibit a unit length and are colored according to the model results.

viscosities in the upper crust below the Tibetan Plateau, which are due to the elevated temperatures there, ultimately resulting from the strongly thickened crust. Rotation of stress orientations around the eastern syntaxis can also be observed.

Stresses in the lower crust of India (Figure 14c) are similar to those at the surface and in the upper crust. In the Tibetan Plateau the distinct E-W directed extension is again observed. In contrast to the surface, we observe that within the lower crust, the Tarim Basin and the Sichuan Basin are compressed. The rest of the Asian continent has low stresses.

Comparing the different layers, large differences exist in the stress orientations and magnitudes. Studies using the thin-sheet approximation to deduce the stress state of the modern India-Asia collision [e.g., *Ghosh et al*., 2006] only find a vertically integrated solution which cannot account for different processes taking place in different layers, and therefore show a generally simplified image in broad and thick zones of active deformation such as Tibet.

Comparisons of model results with measured data (e.g., GPS velocities) or geological observations yield good agreements. Although not all measured data are yet correctly fitted, the overall stress and strength state and the velocity field could be reproduced. Especially differences in the stress, strain, and velocity fields in an orogen on scales smaller than approximately 100 km, such as the elevated stresses in the upper crust at the foot of the Himalaya (Figure 9a), can only be reproduced by applying mechanically layered 3-D models with horizontal heterogeneities. Due to the more realistic 3-D model geometry, it is possible to successfully reproduce the stress pattern of the modern India-Asia collision in agreement with observational constraints: (i) The north-south directed compression of India, (ii) the east-west extension of the Tibetan Plateau, and (iii) the rotation of stress orientations around the eastern syntaxis.

4.1.3. Strain Rates

Strain rates on the surface of the Tibetan Plateau approximately range between 3×10^{-16} and $3 \times 10^{-15}\,s^{-1}$ (Figure 10). These values correspond well with values ranging between 5×10^{-16} and $5 \times 10^{-15}\,s^{-1}$ (~ 15×10^{-9} to $150 \times 10^{-9}\,year^{-1}$) derived by *Kreemer et al*. [2003] for the Tibetan Plateau. As for stresses, increased strain rates also occur at the Himalayan front and around the eastern syntaxis (see section 3.4.3 and Figures 10a and 10b). Such increased strain rates at the border of the Tibetan Plateau, compared to its interior, are reported from studies inferring strain rates from Quaternary fault slip rates [e.g., *Kreemer et al*., 2003].

4.2. Impact of Varying Model Parameters on the Results

We tested the impact of the viscosity of the Indian lower crust by considering values in the range of 10^{21}–10^{24} Pa s. We found that these viscosities all yield similar surface velocities, and thus, all compare equally well to the observed GPS velocities. Varying the viscosity of the Indian lower crust by 3 orders of magnitude has only a minor impact on the surface velocity field. Similarly, strain rates on the model surface only decrease by less than 1 order of magnitude when increasing the Indian lower crustal viscosity by 3 orders of magnitude. Strain rates in the Indian lower crust itself, however, vary by approximately 2 orders of magnitude. This implies that strong variations exist with depth in the deformation field. Furthermore, it is likely that the surface deformation field is not an indicator for deformation at depth. A mechanically coupled (for an Indian lower crustal viscosity of 10^{24} Pa s) or decoupled (for an Indian lower crustal viscosity of 10^{21} Pa s) upper crust and upper lithospheric mantle lead to approximately the same deformation pattern on the surface. Nonetheless, locally stresses and strain rates in adjacent layers are affected by the strength of the Indian lower crust. Indian lower crustal viscosities of 10^{21}–10^{22} Pa s lead to high stresses in the upper crust south of the Tibetan Plateau. These high stresses coincide with the location of the Main Boundary Thrust and the Main Frontal Thrust. The results for different viscosities of the Indian lower crust suggest that comparing model surface velocities with observed GPS values gives no clear indication on the strength and deformation behavior of lower lithospheric levels in general and the Indian lower crust in particular. Horizontal surface velocities are mainly influenced by the boundary conditions and the viscosity of the weak zones.

A more complete analysis of the impact of the model parameters on the model results could be done by a systematic variation of the model parameters of all the model units. However, this computationally extensive exercise is beyond the scope of this study and will be the objective of future work.

4.3. Limitations of the Model

Each step applied for constraining the presented model can be improved as still a number of features of the modern India-Asia orogenic system are unaccounted for

1. The rheology can be elaborated by including plasticity, which is computationally more demanding but could lead to the spontaneous formation of high-strain shear zones, the location of which could be compared to the location of existing thrusts in the modern India-Asian orogenic system. Recent 2-D lithospheric models consider a viscoelastoplastic rheology, thermomechanical coupling and the related thermal softening, and strain localization [e.g., *Burg and Schmalholz*, 2008; *Schmalholz et al*., 2009; *Kaus*, 2010; *Thielmann and Kaus*, 2012]. Such more advanced rheologies and coupling mechanisms are not yet included in our 3-D model.
2. The effect of a power law viscous rheology was only shown exemplary partly because it is computationally expensive but also because the main aim of this study is the investigation of the fundamental impact of mechanical layering and an underthrusting Indian lower crust on the 3-D deformation. *Lechmann et al*. [2011] showed that for a linear viscous rheology and a rigid indenter with no underthrusting, thin-sheet models approximate relatively well the results of mechanically stratified 3-D models and that significant differences between thin-sheet models and 3-D models occur only for power law viscous flow laws. However, for the investigated underthrusting scenario, significant vertical variations of the stress, strain rate, and velocity fields occur already for a linear viscous rheology, indicating that for the investigated scenario thin-sheet models are not applicable even for linear viscous flow laws. Therefore, the first-order impact of mechanical layering and underthrusting is investigated here mainly for linear viscous flow laws because the impact of power law flow laws is expected to be even stronger [*Lechmann et al*., 2011].
3. Including the middle crustal layer of CRUST2.0 would further improve the model geometry, as it was seen that the thickness of the lower crust can have locally a significant impact on the results. This indicates the necessity for a detailed distinction of crustal layers and their respective material properties.
4. In the vertical model dimension, the deep mantle was not accounted for. This is mainly motivated by the fact that this study focuses on instantaneous processes in the lithosphere and that an additional (thick) layer would decrease the model resolution in the lithosphere. Neglecting deeper mantle levels is justifiable, as the model's density distribution is fitted with observed Bouguer anomalies and the isostatic condition of the modern India-Asia orogen should be well reproduced. Due to the instantaneous nature of the simulations, it is not expected that deeper mantle levels absorb significant isostatic compensating movements in such a short time interval.
5. Constraining the density distribution using observed Bouguer anomalies can be improved by (a) new, more densely spaced constraints on the geometry of structures at depth, (b) full 3-D variation of density, for example using petrogenetic grids [e.g., *Hetényi et al*., 2007], and (c) using an automated routine (e.g., Monte Carlo inversions), which will allow testing of more density distributions and yield better fits.
6. Above the underthrusting Indian lower crust seismological surveys postulate the presence of a weak shear zone—the continuation of the Main Himalayan Thrust (MHT) at depth [e.g., *Schulte-Pelkum et al*., 2005; *Nabelek et al*., 2009]. This feature is so far not accounted for in the 3-D numerical model as the investigation of the mechanical stratification was one of the main aims. Furthermore, there is a lack of information regarding its three-dimensional structure. Including this weak zone would allow (a) including a further decoupling interface within the lithosphere, (b) testing the viability of (lower) crustal flow beneath Tibet, (c) testing the impact of material transfer through the MHT on the evolution of the Himalayan wedge, and (d) probably reduce the velocity variation at the surface of the presented models as the thrust likely reduces the resistance at the front of the Himalayan belt.
7. The 3-D model geometry (boundaries between units, distinction of more layers, presence of slabs or their remnants, shape of the underthrusting Indian slab, etc.) can be improved in the future as improved geophysical data sets become available. For example, slabs are not considered in our model (like in essentially all previous models of the India-Asia system). The key question concerning slabs in our model is whether slabs are present that are still attached to the lithosphere or not. If slabs are no longer attached and are instead present at deeper parts of the upper mantle, they will have little to no influence on the lithospheric deformation field as they cannot transmit sufficient forces. If they are attached, on the other hand, it could indeed have an important effect. Recent studies, for example, by *Li and van der Hilst* [2010] and *Li et al*. [2008] (which also discuss older results of *Tilmann et al*. [2003]) conclude "The (continental) parts of

the Indian plate that currently underthrust or subduct below the plateau appear generally detached from the (oceanic) slab fragments that subducted longer ago and that have been detected deeper in the mantle, except perhaps in the central part of the collision zone (80°E–90°E)." The tomographic models of *Priestley et al*. [2006] show underthrusting in the majority of the collision belt but no attached slabs. A clear indication for the presence of a subducting slab comes from seismicity. In the Hindu-Kush region, active seismicity and tomographic models suggest that a slab exists. Underneath Burma, *Li et al*. [2008] show evidence for an eastward subducting slab including active seismicity (up to a depth of ~200 km but not deeper). But as those slabs are essentially perpendicular to the present-day motion direction of India their contribution to the present-day velocity field of India is likely to be minor, although we can of course not exclude that it has some effect on the flow fields at depth. Recent tomographic models thus show that the slabs underneath Tibet are detached rather than attached and are generally found at deeper levels in the mantle. As such, our assumption of ignoring slabs in our models is a reasonable first-order assumption. In the future, increasing computational power will help to numerically resolve these additional features.

8. Velocity boundary conditions are applied on the sides of the model, using the known present-day collision velocity of India with Asia, although the question of the forces driving the India-Asia collision is still subject of ongoing studies (see section 1 and *Lithgow-Bertelloni and Richards* [1998] and *Conrad and Lithgow-Bertelloni* [2004]). If one wishes to study the relative importance of side or bottom forces in a self-consistent manner, one should use a spherical model of the Earth with lateral viscosity variations (as they might induce net rotation), a self-consistent free surface (for topography-driven flow) and high resolution in the crust and lithosphere with realistic changes in the viscosity structure (to resolve, for example, a weak lower crust). This is beyond the subject of this study. Applying the boundary conditions on the sides of the model, i.e., the W-E trending model boundary, implies that the velocity vectors in India point to the north, although in reality they are pointing more toward NNE. Future model configurations should be adapted to this fact.
9. Our thermal model does not consider large magmatic intrusions such as the Trans-Himalayan Batholith [e.g., *Copeland et al*., 1995]. The Trans-Himalayan Batholith mostly formed prior to the collision of India with the Tibetan Plateau. Its emplacement is thought to have happened between 110 and 40 Ma. Therefore, most of its heat input to the system has already happened, and the Trans-Himalayan have likely no major effect on the current thermal state of the plateau [e.g., *Pollack et al*., 1993; *Hu et al*., 2000]. When considering heat flow values measured on the Tibetan Plateau, they are (a) scarce, (b) show normal to high values, and (c) they all sample N-S trending extensional grabens or geothermal areas [e.g., *Hetényi et al*., 2011]. Therefore, the high heat flow values are not representative of the entire plateau's thermal state, which remains fairly unknown and necessarily approximated in any model.

5. Conclusions

We investigated the fundamental controls of the mechanical layering of the lithosphere and of the underthrusting of the Indian lower crust on the deformation in the modern India-Asia collisional system with 3-D thermomechanical numerical models. The model geometry and parameters are constrained by available geophysical data. The main conclusions for the dynamics of the modern India-Asia orogen are (1) Flow laws typically used to describe the rheology of the continental lithosphere yield a good constraint of the continental viscosity distribution because viscous stresses are consistent with GPE-induced stresses, and model velocities are consistent with surface GPS velocities. (2) Differences in the density distribution, which agree to a similar degree with observed Bouguer anomalies, have a relatively minor impact on the velocity, strain rate, and stress fields. (3) Varying the Indian lower crustal viscosity by 3 orders of magnitude leads to similar fits of horizontal surface and GPS velocities. Significant variations in the Indian lower crustal viscosity cause minor variations in the surface velocity field and moderate variations in the strain rate field. These results suggest that inferences made only from surface velocities and strain rates are insufficient to constrain the deformation at depth or the degree of mechanical coupling of the lithosphere. (4) The presence of large-scale strike-slip faults has a crucial impact on model results, especially on the surface velocity field. A relatively weak Sagaing Fault zone and a relatively strong Quetta-Chaman Fault zone provide results that best fit observations. (5) Lateral variations in GPE can cause locally significant tectonic overpressure (i.e., difference between pressure and lithostatic pressure) in mechanically strong layers. The maximal tectonic overpressure in the Indian lower crust caused only by GPE variations (static scenario) is approximately 500 MPa and approximately 800 MPa if also indentation takes place (dynamic scenario).

Appendix A: Governing Equations and Numerical Method

The 3-D model is based on the continuum mechanics conservation equations. The conservation equation representing the momentum balance is

$$\frac{\partial \sigma_{ij}}{\partial x_j} = \rho g a_i \tag{A1}$$

with σ_{ij} being the total stress tensor, ρ the density, g the gravity, and $\vec{a} = (0, 0, 1)^T$. Indices i, j run from 1 to 3 and refer to the three spatial coordinates x, y, z, respectively. According to the summation convention, repeated indices are summed. The superscript T indicates the transpose of a vector or matrix.

The incompressibility condition, with velocity vector $\vec{v} = (v_x, v_y, v_z)^T$ and $\nabla = \left(\frac{\partial}{\partial x}, \frac{\partial}{\partial y}, \frac{\partial}{\partial z}\right)^T$, is

$$\nabla^T \cdot \vec{v} = 0 \tag{A2}$$

with the symbol $\cdot$ representing a scalar product.

The deviatoric stress tensor is

$$\tau_{ij} = \sigma_{ij} + \delta_{ij} p \tag{A3}$$

where $p = -\frac{1}{3}\left(\sigma_{xx} + \sigma_{yy} + \sigma_{zz}\right)$ is the pressure (negative of mean stress) and δ_{ij} is the Kronecker delta.

We apply the constitutive relation

$$\tau_{ij} = 2\mu\ \dot{\varepsilon}_{ij} \tag{A4}$$

where $\dot{\varepsilon}_{ij} = \frac{1}{2}\left(\frac{\partial v_i}{\partial x_j} + \frac{\partial v_j}{\partial x_i}\right)$ are the components of the strain rate tensor and $\dot{\varepsilon}_{II} = \sqrt{\frac{1}{2}\ \dot{\varepsilon}_{ij}\ \dot{\varepsilon}_{ij}}$ is the square root of the second invariant of the strain rate tensor. The viscosity μ is defined in equation (1).

Substituting equations (A3) and (A4) into equation (A1) leads to

$$B^T D B\ \vec{v} - \nabla p = \rho g \vec{a}, \tag{A5}$$

where

$$B = \begin{bmatrix} \frac{\partial}{\partial x} & 0 & 0 \\ 0 & \frac{\partial}{\partial y} & 0 \\ 0 & 0 & \frac{\partial}{\partial z} \\ \frac{\partial}{\partial y} & \frac{\partial}{\partial x} & 0 \\ 0 & \frac{\partial}{\partial z} & \frac{\partial}{\partial y} \\ \frac{\partial}{\partial z} & 0 & \frac{\partial}{\partial x} \end{bmatrix} \text{ and } D = \begin{bmatrix} 2\mu & 0 & 0 & 0 & 0 & 0 \\ 0 & 2\mu & 0 & 0 & 0 & 0 \\ 0 & 0 & 2\mu & 0 & 0 & 0 \\ 0 & 0 & 0 & \mu & 0 & 0 \\ 0 & 0 & 0 & 0 & \mu & 0 \\ 0 & 0 & 0 & 0 & 0 & \mu \end{bmatrix}.$$

Equations (A2) and (A5) represent the four governing equations in 3-D for the four unknowns v_x, v_y, v_z, and p. These equations are discretized using a standard mixed finite element method (FEM) [*Hughes*, 1987; *Brezzi and Fortin*, 1991]. The domain is discretized with hexahedral elements, using the element type Q_2P_{-1} which consists of a triquadratic basis function for velocity and a piecewise discontinuous linear basis function for pressure [*Brezzi and Fortin*, 1991]. Following the discretization of the Stokes equations, we obtain the following discrete system:

$$\begin{bmatrix} K & Q \\ Q^T & 0 \end{bmatrix} \begin{Bmatrix} \vec{v} \\ \vec{p} \end{Bmatrix} = \begin{Bmatrix} \vec{f} \\ 0 \end{Bmatrix} \tag{A6}$$

with $K = \iiint \widetilde{B}^T D \widetilde{B}\, dx dy dz$ the discrete gradient of the stress tensor, $Q = -\iiint B_G^T N_p\, dx dy dz$ the discrete gradient, Q^T the discrete divergence, and $\vec{f} = \iiint N_v^T \rho g \vec{a}\, dx dy dz$ the discrete body force. Matrices $\widetilde{B}$ and B_G contain spatial derivatives of the velocity shape functions. Vectors N_p , N_v contain the pressure and the velocity shape functions.

The mixed finite element method described above has been implemented within the code LaMEM (Lithosphere and Mantle Evolution Model) [*Schmeling et al*., 2008; *Lechmann et al*., 2011]. LaMEM is a parallel (distributed memory) FEM code developed using the Portable, Extensible Toolkit for Scientific Computation library [*Balay et al*., 2009], which provides a flexible mechanism to change and configure the solution strategy used to compute the discrete velocity and pressure from equation (A6).

Solution of the numerical problem is achieved with an iterative approach. The system of equations is solved with a Schur complement reduction based geometric multigrid solver [*Briggs et al*., 2000] which requires a hierarchy of finite element meshes and a coarse grid operator on each. As Krylov method FGMRES is employed [*Saad*, 2003]. Except for the coarsest level, where the direct solver SuperLU is used [*Li*, 2005], for the other multigrid levels, four iterations of FGMRES preconditioned with block ILU are used.

Acknowledgments

We thank two anonymous reviewers and the Associate Editor for their reviews. We thank ETH Zurich and the University of Lausanne for supporting this work. S.M.L. was supported by ETH grant 0-20497-08. B.K. received funding from the European Research Council under the European Union's Seventh Framework Programme (FP7/2007–2013)/ERC grant agreement 258830. Furthermore, we thank the University of Lausanne for the use of the clusters "BlueGene/P" and "Achilles".

References

Acton, C. E., K. Priestley, S. Mitra, and V. K. Gaur (2010), Crustal structure of the Darjeeling–Sikkim Himalaya and southern Tibet, *Geophys. J. Int.*, *184*, 829–852.

Afonso, J. C., and G. Ranalli (2004), Crustal and mantle strengths in continental lithosphere: Is the jelly sandwich model obsolete?, *Tectonophysics*, *394*(3-4), 221–232.

Afonso, J. C., G. Ranalli, and M. Fernandez (2007), Density structure and buoyancy of the oceanic lithosphere revisited, *Geophys. Res. Lett.*, *34*, L10302, doi:10.1029/2007GL029515.

Allegre, C. J., et al. (1984), Structure and evolution of the Himalaya-Tibet orogenic belt, *Nature*, *307*(5946), 17–22.

Argand, E. (1924), La tectonique de l'Asie, in *Comptes Rendu 3? Congress International Geologie (Liege)*, edited by A. V. Carozzi, pp. 218, Hafner Press, New York.

Armijo, R., P. Tapponnier, J. L. Mercier, and T. L. Han (1986), Quaternary extension in Southern Tibet—Field observations and tectonic implications, *J. Geophys. Res.*, *91*(B14), 13,803–13,872.

Balay, S., K. Buschelman, W. D. Gropp, D. Kaushik, M. G. Knepley, L. Curfman McInnes, B. F. Smith, and H. Zhang (2009), PETSc web page. [Available at http://www.mcs.anl.gov/petsc.]

Banerjee, P., R. Burgmann, B. Nagarajan, and E. Apel (2008), Intraplate deformation of the Indian subcontinent, *Geophys. Res. Lett.*, *35*, L18301, doi:10.1029/2008GL035468.

Batchelor, G. K. (1967), *An Introduction to Fluid Dynamics*, Cambridge Univ. Press, Cambridge, U.K.

Beaumont, C., R. A. Jamieson, M. H. Nguyen, and B. Lee (2001), Himalayan tectonics explained by extrusion of a low-viscosity crustal channel coupled to focused surface denudation, *Nature*, *414*(6865), 738–742.

Beaumont, C., R. A. Jamieson, M. H. Nguyen, and S. Medvedev (2004), Crustal channel flows: 1. Numerical models with applications to the tectonics of the Himalayan-Tibetan orogen, *J. Geophys. Res.*, *109*, B06406, doi:10.1029/2003JB002809.

Becker, T. W. (2006), On the effect of temperature and strain-rate dependent viscosity on global mantle flow, net rotation, and plate-driving forces, *Geophys. J. Int.*, *167*(2), 943–957.

Bird, P. (2003), An updated digital model of plate boundaries, *Geochem. Geophys. Geosyst.*, *4*(3), 1027, doi:10.1029/2001GC000252.

Blakely, R. J. (1996), *Potential Theory in Gravity and Magnetic Applications*, Cambridge Univ. Press, Cambridge, U.K.

Brezzi, F., and M. Fortin (1991), *Mixed and Hybrid Finite Element Methods*, Springer Verlag, New York.

Briggs, W. L., V. E. Henson, and S. F. Cormick (2000), A multigrid tutorial, Philadelphia. [Available online at http://www.math.ust.hk/~mawang/teaching/math532/mgtut.pdf.]

Burg, J. P., and G. M. Chen (1984), Tectonics and structural zonation of southern Tibet, China, *Nature*, *311*(5983), 219–223.

Burg, J. P., and Y. Podladchikov (1999), Lithospheric scale folding: Numerical modelling and application to the Himalayan syntaxes, *Int. J. Earth Sci.*, *88*(2), 190–200.

Burg, J. P., and Y. Podladchikov (2000), From buckling to asymmetric folding of the continental lithosphere: Numerical modelling and application to the Himalayan syntaxes, in *Tectonics of the Nanga Parbat Syntaxis and the Western Himalaya*, vol. 170, edited by P. J. Treloar, M. P. Searle, and M. Q. Jan, pp. 219–236, Geological Society, London, U.K.

Burg, J. P., and S. M. Schmalholz (2008), Viscous heating allows thrusting to overcome crustal-scale buckling: Numerical investigation with application to the Himalayan syntaxes, *Earth Planet. Sci. Lett.*, *274*(1–2), 189–203.

Burov, E. B. (2010), The equivalent elastic thickness (T-e), seismicity and the long-term rheology of continental lithosphere: Time to burn-out "creme brulee"? Insights from large-scale geodynamic modeling, *Tectonophysics*, *484*(1-4), 4–26.

Burov, E. B., L. I. Lobkovsky, S. Cloetingh, and A. M. Nikishin (1993), Continental lithosphere folding in central-Asia 2. Constraints from gravity and topography, *Tectonophysics*, *226*(1-4), 73–87.

Carter, N. L., and M. C. Tsenn (1987), Flow properties of continental lithosphere, *Tectonophysics*, *136*(1-2), 27–63.

Cattin, R., G. Martelet, P. Henry, J. P. Avouac, M. Diament, and T. R. Shakya (2001), Gravity anomalies, crustal structure and thermo-mechanical support of the Himalaya of central Nepal, *Geophys. J. Int.*, *147*(2), 381–392.

Clark, M. K., and L. H. Royden (2000), Topographic ooze: Building the eastern margin of Tibet by lower crustal flow, *Geology*, *28*(8), 703–706.

Clark, M. K., J. W. M. Bush, and L. H. Royden (2005), Dynamic topography produced by lower crustal flow against rheological strength heterogeneities bordering the Tibetan Plateau, *Geophys. J. Int.*, *162*(2), 575–590.

Coblentz, D. D., R. M. Richardson, and M. Sandiford (1994), On the gravitational potential of the Earth's lithosphere, *Tectonics*, *13*(4), 929–945.

Conrad, C. P., and C. Lithgow-Bertelloni (2004), The temporal evolution of plate driving forces: Importance of "slab suction" versus "slab pull" during the Cenozoic, *J. Geophys. Res.*, *109*, B10407, doi:10.1029/2004JB002991.

Cook, K. L., and L. H. Royden (2008), The role of crustal strength variations in shaping orogenic plateaus, with application to Tibet, *J. Geophys. Res.*, *113*, B08407, doi:10.1029/2007JB005457.

Copeland, P., T. M. Harrison, P. Yun, W. S. F. Kidd, M. Roden, and Y. Q. Zhang (1995), Thermal evolution of the Gangdese batholith, southern Tibet—A history of episodic unroofing, *Tectonics*, *14*(2), 223–236, doi:10.1029/94tc01676.

Copley, A., and D. McKenzie (2007), Models of crustal flow in the India-Asia collision zone, *Geophys. J. Int.*, *169*(2), 683–698.

Copley, A., J. P. Avouac, and B. P. Wernicke (2011), Evidence for mechanical coupling and strong Indian lower crust beneath southern Tibet, *Nature*, *472*(7341), 79–81.

Dayem, K. E., G. A. Houseman, and P. Molnar (2009a), Localization of shear along a lithospheric strength discontinuity: Application of a continuous deformation model to the boundary between Tibet and the Tarim Basin, *Tectonics*, *28*, TC3002, doi:10.1029/2008TC002264.
Dayem, K. E., P. Molnar, M. K. Clark, and G. A. Houseman (2009b), Far-field lithospheric deformation in Tibet during continental collision, *Tectonics*, *28*, TC6005, doi:10.1029/2008TC002344.
DeCelles, P. G., D. M. Robinson, and G. Zandt (2002), Implications of shortening in the Himalayan fold-thrust belt for uplift of the Tibetan Plateau, *Tectonics*, *21*(6), 1062, doi:10.1029/2001TC001322.
Dziewonski, A. M., and D. L. Anderson (1981), Preliminary reference Earth model, *Phys. Earth Planet. Inter.*, *25*(4), 297–356.
Ellis, S. (1996), Forces driving continental collision: Reconciling indentation and mantle subduction tectonics, *Geology*, *24*(8), 699–702.
England, P., and G. Houseman (1985), Role of lithospheric strength heterogeneities in the tectonics of Tibet and neighboring regions, *Nature*, *315*(6017), 297–301.
England, P., and G. Houseman (1986), Finite strain calculations of continental deformation 2. Comparison with the India-Asia collision zone, *J. Geophys. Res.*, *91*(B3), 3664–3676.
England, P., and D. McKenzie (1982), A thin viscous sheet model for continental deformation, *Geophys. J. R. Astron. Soc.*, *70*(2), 295–321.
England, P., and P. Molnar (1997a), Active deformation of Asia: From kinematics to dynamics, *Science*, *278*(5338), 647–650.
England, P., and P. Molnar (1997b), The field of crustal velocity in Asia calculated from Quaternary rates of slip on faults, *Geophys. J. Int.*, *130*(3), 551–582.
Fleitout, L., and C. Froidevaux (1982), Tectonics and topography for a lithosphere containing density heterogeneities, *Tectonics*, *1*(1), 21–56.
Flesch, L. M., and R. Bendick (2012), The relationship between surface kinematics and deformation of the whole lithosphere, *Geology*, *40*(8), 711–714.
Flesch, L. M., A. J. Haines, and W. E. Holt (2001), Dynamics of the India-Eurasia collision zone, *J. Geophys. Res.*, *106*(B8), 16,435–16,460.
Flesch, L. M., W. E. Holt, P. G. Silver, M. Stephenson, C. Y. Wang, and W. W. Chan (2005), Constraining the extent of crust-mantle coupling in central Asia using GPS, geologic, and shear wave splitting data, *Earth Planet. Sci. Lett.*, *238*(1-2), 248–268.
Gan, W. J., P. Z. Zhang, Z. K. Shen, Z. J. Niu, M. Wang, Y. G. Wan, D. M. Zhou, and J. Cheng (2007), Present-day crustal motion within the Tibetan Plateau inferred from GPS measurements, *J. Geophys. Res.*, *112*, B08416, doi:10.1029/2005JB004120.
Gansser, A. (1964), *Geology of the Himalayas*, pp. 289, Wiley Interscience, London/New York/Sydney.
Ghosh, A., W. E. Holt, L. M. Flesch, and A. J. Haines (2006), Gravitational potential energy of the Tibetan Plateau and the forces driving the Indian Plate, *Geology*, *34*(5), 321–324.
Ghosh, A., W. E. Holt, and L. M. Flesch (2009), Contribution of gravitational potential energy differences to the global stress field, *Geophys. J. Int.*, *179*(2), 787–812.
Hammer, P., T. Berthet, G. Hetenyi, R. Cattin, D. Drukpa, J. Chophel, S. M. Lechmann, N. Le Moigne, C. Champollion, and E. Doerflinger (2013), Flexure of the India Plate underneath the Bhutan Himalaya, *Geophys. Res. Lett.*, *40*, 4225–4230, doi:10.1002/grl.50793.
Hauck, M. L., K. D. Nelson, L. D. Brown, W. J. Zhao, and A. R. Ross (1998), Crustal structure of the Himalayan orogen at similar to 90 degrees east longitude from Project INDEPTH deep reflection profiles, *Tectonics*, *17*(4), 481–500.
Heidbach, O., M. Tingay, A. Barth, J. Reinecker, D. Kurfess, and B. Mueller (2008), The World Stress Map database release 2008.
Hetényi, G. (2007), Evolution of deformation of the Himalayan prism: From imaging to modelling, PhD thesis, École Normale Supérieure-Université Paris-Sud XI, Paris, France.
Hetényi, G., R. Cattin, J. Vergne, and J. L. Nabelek (2006), The effective elastic thickness of the India Plate from receiver function imaging, gravity anomalies and thermomechanical modelling, *Geophys. J. Int.*, *167*(3), 1106–1118.
Hetényi, G., R. Cattin, F. Brunet, L. Bollinger, J. Vergne, J. Nabelek, and M. Diament (2007), Density distribution of the India plate beneath the Tibetan Plateau: Geophysical and petrological constraints on the kinetics of lower-crustal eclogitization, *Earth Planet. Sci. Lett.*, *264*(1-2), 226–244.
Hetényi, G., J. Vergne, L. Bollinger, and R. Cattin (2011), Discontinuous low-velocity zone in southern Tibet questions the viability of channel flow model, in *Growth and Collapse of the Tibetan Plateau*, vol. 353, edited by R. Gloaguen and L. Ratschbacher, Spec. Pub. series, pp. 99–108, Geological Society of London, London, doi:10.1144/SP353.6.
Houseman, G., and P. England (1986), Finite strain calculations of continental deformation 1. Method and general results for convergent zones, *J. Geophys. Res.*, *91*(B3), 3651–3663.
Hu, S. B., L. J. He, and J. Y. Wang (2000), Heat flow in the continental area of China: A new data set, *Earth Planet. Sci. Lett.*, *179*(2), 407–419, doi:10.1016/s0012-821x(00)00126-6.
Hughes, T. J. R. (1987), *The Finite Element Method*, Dover Publications, Inc., Mineola, N.Y.
Jackson, J. (2002), Strength of the continental lithosphere: Time to abandon the jelly sandwich?, *GSA Today*, *12*, 4–10.
Jones, C. H., J. R. Unruh, and L. J. Sonder (1996), The role of gravitational potential energy in active deformation in the southwestern United States, *Nature*, *381*(6577), 37–41.
Kaus, B. (2010), Factors that control the angle of shear bands in geodynamic numerical models of brittle deformation, *Tectonophysics*, *484*, 36–47.
Kind, R., et al. (2002), Seismic images of crust and upper mantle beneath Tibet: Evidence for Eurasian Plate subduction, *Science*, *298*(5596), 1219–1221.
Kreemer, C., W. E. Holt, and A. J. Haines (2003), An integrated global model of present-day plate motions and plate boundary deformation, *Geophys. J. Int.*, *154*(1), 8–34.
Laske, G., G. Masters, and C. Reif (2002), Crust 2.0: A new global crustal model at 2×2 degrees.
Le Dain, A. Y., P. Tapponnier, and P. Molnar (1984), Active faulting and tectonics of Burma and surrounding regions, *J. Geophys. Res.*, *89*(Nb1), 453–472.
Lechmann, S. M., D. A. May, B. J. P. Kaus, and S. M. Schmalholz (2011), Comparing thin-sheet models with 3-D multilayer models for continental collision, *Geophys. J. Int.*, *187*(1), 10–33.
Li, X. S. (2005), An overview of SuperLU: Algorithms, implementation, and user interface, *ACM Trans. Math. Software*, *31*, 302–325.
Li, A. B., and B. Mashele (2009), Crustal structure in the Pakistan Himalaya from teleseismic receiver functions, *Geochem. Geophys. Geosyst.*, *10*, Q12010, doi:10.1029/2009GC002700.
Li, C., and R. D. van der Hilst (2010), Structure of the upper mantle and transition zone beneath Southeast Asia from traveltime tomography, *J. Geophys. Res.*, *115*, B07308, doi:10.1029/2009jb006882.
Li, C., R. D. Van der Hilst, A. S. Meltzer, and E. R. Engdahl (2008), Subduction of the Indian lithosphere beneath the Tibetan Plateau and Burma, *Earth Planet. Sci. Lett.*, *274*(1-2), 157–168.
Lithgow-Bertelloni, C., and M. A. Richards (1998), The dynamics of Cenozoic and Mesozoic plate motions, *Rev. Geophys.*, *36*(1), 27–78.

Liu, M., and Y. Q. Yang (2003), Extensional collapse of the Tibetan Plateau: Results of three-dimensional finite element modeling, *J. Geophys. Res.*, *108*(B8), 2361, doi:10.1029/2002JB002248.
Mancktelow, N. S. (2008), Tectonic pressure: Theoretical concepts and modelled examples, *Lithos*, *103*(1-2), 149–177.
McKenzie, D. P. (1972), Plate tectonics, in *The Nature of the Solid Earth*, edited by E. C. Robertson, pp. 323–360, McGraw-Hill, New York.
McKenzie, D., J. Jackson, and K. Priestley (2005), Thermal structure of oceanic and continental lithosphere, *Earth Planet. Sci. Lett.*, *233*(3-4), 337–349.
Meade, B. J. (2007), Present-day kinematics at the India-Asia collision zone, *Geology*, *35*(1), 81–84.
Medvedev, S. E., and Y. Y. Podladchikov (1999a), New extended thin-sheet approximation for geodynamic applications—I. Model formulation, *Geophys. J. Int.*, *136*(3), 567–585.
Medvedev, S. E., and Y. Y. Podladchikov (1999b), New extended thin-sheet approximation for geodynamic applications—II. Two-dimensional examples, *Geophys. J. Int.*, *136*(3), 586–608.
Meigs, A. J., D. W. Burbank, and R. A. Beck (1995), Middle-late Miocene (.10 Ma) formation of the Main Boundary Thrust in the western Himalaya, *Geology*, *23*, 423–426.
Michel, G. W., M. Becker, D. Angermann, C. Reigber, and E. Reinhart (2000), Crustal motion in E- and SE-Asia from GPS measurements, *Earth Planets Space*, *52*(10), 713–720.
Moghadam, R. H., C. A. Trepmann, B. Stockhert, and J. Renner (2010), Rheology of synthetic omphacite aggregates at high pressure and high temperature, *J. Petrol.*, *51*(4), 921–945, doi:10.1093/petrology/egq006.
Molnar, P., and H. Lyon-Caen (1988), Some simple physical aspects of the support, structure, and evolution of mountain belts, *Geol. Soc. Am. Spec. Pap.*, *218*, 179–207.
Molnar, P., and P. Tapponnier (1975), Cenozoic tectonics of Asia—Effects of a continental collision, *Science*, *189*(4201), 419–426.
Molnar, P., and P. Tapponnier (1981), A possible dependence of tectonic strength on the age of the crust in Asia, *Earth Planet. Sci. Lett.*, *52*(1), 107–114.
Molnar, P., P. England, and J. Martinod (1993), Mantle dynamics, uplift of the Tibetan Plateau, and the Indian Monsoon, *Rev. Geophys.*, *31*(4), 357–396.
Nabelek, J., G. Hetenyi, J. Vergne, S. Sapkota, B. Kafle, M. Jiang, H. P. Su, J. Chen, B. S. Huang, and H.-C. Team (2009), Underplating in the Himalaya-Tibet collision zone revealed by the Hi-CLIMB experiment, *Science*, *325*(5946), 1371–1374.
Patriat, P., and J. Achache (1984), India Eurasia collision chronology has implications for crustal shortening and driving mechanism of plates, *Nature*, *311*(5987), 615–621.
Paul, J., et al. (2001), The motion and active deformation of India, *Geophys. Res. Lett.*, *28*(4), 647–650.
Petrini, K., and Y. Podladchikov (2000), Lithospheric pressure-depth relationship in compressive regions of thickened crust, *J. Metamorph. Geol.*, *18*(1), 67–77.
Pollack, H. N., S. J. Hurter, and J. R. Johnson (1993), Heat-flow from the Earth's interior—Analysis of the global data set, *Rev. Geophys.*, *31*(3), 267–280, doi:10.1029/93rg01249.
Priestley, K., E. Debayle, D. McKenzie, and S. Pilidou (2006), Upper mantle structure of eastern Asia from multimode surface waveform tomography, *J. Geophys. Res.*, *111*, B10304, doi:10.1029/2005JB004082.
Priestley, K., J. Jackson, and D. McKenzie (2008), Lithospheric structure and deep earthquakes beneath India, the Himalaya and southern Tibet, *Geophys. J. Int.*, *172*(1), 345–362.
Quittmeyer, R. C., and K. H. Jacob (1979), Historical and modern seismicity of Pakistan, Afghanistan, northwestern India, and southeastern Iran, *Bull. Seismol. Soc. Am.*, *69*(3), 773–823.
Rai, S. S., K. Priestley, V. K. Gaur, S. Mitra, M. P. Singh, and M. Searle (2006), Configuration of the Indian Moho beneath the NW Himalaya and Ladakh, *Geophys. Res. Lett.*, *33*, L15308, doi:10.1029/2006GL026076.
Ranalli, G. (1995), *Rheology of the Earth*, 2nd ed., pp. 413, Chapman & Hall, London, U.K.
Robert, A., J. Zhu, J. Vergne, R. Cattin, L. S. Chan, G. Wittlinger, G. Herquel, J. de Sigoyer, M. Pubellier, and L. D. Zhu (2010), Crustal structures in the area of the 2008 Sichuan earthquake from seismologic and gravimetric data, *Tectonophysics*, *491*(1-4), 205–210.
Royden, L. H., B. C. Burchfiel, and R. D. van der Hilst (2008), The geological evolution of the Tibetan Plateau, *Science*, *321*(5892), 1054–1058.
Saad, Y. (2003), *Iterative Methods for Sparse Linear Systems*, 2nd ed., SIAM, Philadelphia.
Schmalholz, S. M., and Y. Y. Podladchikov (2013), Tectonic overpressure in weak crustal-scale shear zones and implications for the exhumation of high-pressure rocks, *Geophys. Res. Lett.*, *40*, 1984–1988, doi:10.1002/grl.50417.
Schmalholz, S. M., B. J. P. Kaus, and J. P. Burg (2009), Stress-strength relationship in the lithosphere during continental collision, *Geology*, *37*(9), 775–778, doi:10.1130/g25678a.1.
Schmeling, H., et al. (2008), A benchmark comparison of spontaneous subduction models—Towards a free surface, *Phys. Earth Planet. Inter.*, *171*, 198–223.
Schulte-Pelkum, V., G. Monsalve, A. Sheehan, M. R. Pandey, S. Sapkota, R. Bilham, and F. Wu (2005), Imaging the Indian subcontinent beneath the Himalaya, *Nature*, *435*(7046), 1222–1225.
Shi, D., et al. (2004), Detection of southward intracontinental subduction of Tibetan lithosphere along the Bangong-Nujiang suture by P-to-S converted waves, *Geology*, *32*(3), 209–212.
Singh, A., M. R. Kumar, and P. S. Raju (2010), Seismic structure of the underthrusting Indian crust in Sikkim Himalaya, *Tectonics*, *29*, TC6021, doi:10.1029/2010TC002722.
Szeliga, W., R. Bilham, D. M. Kakar, and S. H. Lodi (2012), Interseismic strain accumulation along the western boundary of the Indian subcontinent, *J. Geophys. Res.*, *117*, B08404, doi:10.1029/2011JB008822.
Tapponnier, P., and P. Molnar (1976), Slip-line field-theory and large-scale continental tectonics, *Nature*, *264*(5584), 319–324.
Taylor, M., A. Yin, F. J. Ryerson, P. Kapp, and L. Ding (2003), Conjugate strike-slip faulting along the Bangong-Nujiang suture zone accommodates coeval east-west extension and north-south shortening in the interior of the Tibetan Plateau, *Tectonics*, *22*(4), 1044, doi:10.1029/2002TC001361.
Thielmann, M., and B. J. P. Kaus (2012), Shear heating induced lithospheric-scale localization: Does it result in subduction?, *Earth Planet. Sci. Lett.*, *359*, 1–13, doi:10.1016/j.epsl.2012.10.002.
Tilmann, F., J. Ni, and I. I. S. Team (2003), Seismic imaging of the downwelling Indian lithosphere beneath central Tibet, *Science*, *300*(5624), 1424–1427, doi:10.1126/science.1082777.
U.S. Geological Survey (2012), USGS earthquake database. [Available at http://earthquake.usgs.gov/earthquakes/eqarchives/epic/epic_rect.php.]
Vergne, J., G. Wittlinger, Q. A. Hui, P. Tapponnier, G. Poupinet, J. Mei, G. Herquel, and A. Paul (2002), Seismic evidence for stepwise thickening of the crust across the NE Tibetan Plateau, *Earth Planet. Sci. Lett.*, *203*(1), 25–33.

Vergnolle, M., E. Calais, and L. Dong (2007), Dynamics of continental deformation in Asia, *J. Geophys. Res.*, *112*, B11403, doi:10.1029/2006JB004807.

Wang, C. Y., L. M. Flesch, P. G. Silver, L. J. Chang, and W. W. Chan (2008a), Evidence for mechanically coupled lithosphere in central Asia and resulting implications, *Geology*, *36*(5), 363–366.

Wang, J., Z. R. Ye, and H. K. He (2008b), Three-dimensional mechanical modeling of large-scale crustal deformation in China constrained by the GPS velocity field, *Tectonophysics*, *446*(1-4), 51–60.

Wang, C. Y., L. P. Zhu, H. Lou, B. S. Huang, Z. X. Yao, and X. H. Luo (2010), Crustal thicknesses and Poisson's ratios in the eastern Tibetan Plateau and their tectonic implications, *J. Geophys. Res.*, *115*, B11301, doi:10.1029/2010JB007527.

Wittlinger, G., V. Farra, and J. Vergne (2004a), Lithospheric and upper mantle stratifications beneath Tibet: New insights from Sp conversions, *Geophys. Res. Lett.*, *31*, L19615, doi:10.1029/2004GL020955.

Wittlinger, G., J. Vergne, P. Tapponnier, V. Farra, G. Poupinet, M. Jiang, H. Su, G. Herquel, and A. Paul (2004b), Teleseismic imaging of subducting lithosphere and Moho offsets beneath western Tibet, *Earth Planet. Sci. Lett.*, *221*(1-4), 117–130.

Wittlinger, G., V. Farra, G. Hetenyi, J. Vergne, and J. Nabelek (2009), Seismic velocities in southern Tibet lower crust: A receiver function approach for eclogite detection, *Geophys. J. Int.*, *177*(3), 1037–1049.

Yang, Y. Q., and M. Liu (2009), Crustal thickening and lateral extrusion during the Indo-Asian collision: A 3D viscous flow model, *Tectonophysics*, *465*(1-4), 128–135.

Zhang, P. Z., Z. Shen, M. Wang, W. J. Gan, R. Burgmann, and P. Molnar (2004), Continuous deformation of the Tibetan Plateau from Global Positioning System data, *Geology*, *32*(9), 809–812.

Zhang, Z. J., Y. H. Wang, Y. Chen, G. A. Houseman, X. B. Tian, E. R. Wang, and J. W. Teng (2009), Crustal structure across Longmenshan Fault belt from passive source seismic profiling, *Geophys. Res. Lett.*, *36*, L17310, doi:10.1029/2009GL039580.

Zhao, J. M., et al. (2010), The boundary between the Indian and Asian tectonic plates below Tibet, *Proc. Natl. Acad. Sci. U.S.A.*, *107*(25), 11,229–11,233.